Hindawi Publishing Corporation
Journal of Nanotechnology
Volume 2012, Article ID 645931, 27 pages
doi:10.1155/2012/645931

Review Article

Self-Organized One-Dimensional TiO_2 Nanotube/Nanowire Array Films for Use in Excitonic Solar Cells: A Review

Ningzhong Bao,[1] Xinjian Feng,[2] and Craig A. Grimes[1]

[1] *State Key of Laboratory of Materials-Oriented Chemical Engineering, Nanjing University of Technology, Nanjing, Jiangsu 210009, China*
[2] *Flux Photon Corporation, 617 Hutton Street, Raleigh, NC 27606, USA*

Correspondence should be addressed to Craig A. Grimes, craig.grimes40@gmail.com

Received 20 June 2011; Accepted 23 August 2011

Academic Editor: Qihua Xiong

We review the use of self-assembled, vertically oriented one-dimensional (1D) titania nanowire and nanotube geometries in several third-generation excitonic solar cell designs including those based upon bulk heterojunction, ordered heterojunction, Förster resonance energy transfer (FRET), and liquid-junction dye-sensitized solar cells (DSSCs).

1. Introduction

Third-generation photovoltaics encompass a variety of designs including liquid-based dye-sensitized (Grätzel) solar cells, solid-state bulk heterojunction solar cells [1–6], ordered heterojunction solar cells [7, 8], Förster resonance energy transfer- (FRET-) based solar cells [9–14], and organic solar cells [15, 16]. Liquid-based dye-sensitized solar cells (DSSCs) utilizing for a photoanode a dye-coated layer of TiO_2 nanoparticles have reached efficiencies of over 11% [17], but there are concerns with respect to manufacturing photovoltaic panels with a liquid redox electrolyte. Solid-state organic solar cells are easy to handle and manufacture, and have demonstrated efficiencies ranging from 2 to 8.13% [18–20]. Other 3rd generation photovoltaic designs include plasmonic resonance devices [21], quantum dot and, hopefully, multiple exciton devices [22, 23].

Various nanostructures have been used as a means of energy conversion enhancement in 3rd generation solar cells. These structures can be classified into four types: (a) Nanocomposite (3-dimensional), (b) quantum well (2-dimensional), (c) nanowire and nanotubes (1-dimensional, 1D), and (d) nanoparticles (0-dimensional). Our interest in this paper is the photovoltaic application of self-assembled TiO_2-based 1D nanostructures. Self-organized TiO_2 nanowires/nanotubes arrays [24, 25] vertically oriented on a transparent conducting oxide (TCO) substrate offer numerous benefits such as large surface area for dye sensitization resulting in enhanced light harvesting, easy transfer of electrons injected from photon excited dye, vectorial (directed) charge transport to the electrical contact, and a readily assessable space for intercalation of the redox electrolyte or p-type semiconductor. However, while self-assembled vertically oriented 1D titania nanoarchitectured films offer great potential for enhancing 3rd generation photovoltaic efficiencies to date, such films have not yet been achieved. There is, to date, something always lacking in such fields, be it poor crystallinity of the electron transporting backbone which results in poor charge transport, damage to the transparent conductive oxide coating which increases the series resistance and/or reduces film transmission, or low surface area which limits the amount of light that can be absorbed.

Promising self-assembled 1D titania architectures are films comprised of vertically oriented nanotubes or nanowires. TiO_2 nanotube arrays, on fluorine doped tin oxide-(FTO-) coated glass, of desired pore size and length can be achieved by anodic oxidation [26, 27], while vertically aligned TiO_2 nanowire films can be achieved via a hydrothermal process [24, 25, 28, 29]. The length and pore size of the nanotube arrays can be easily controlled by choosing a suitable anodization electrolyte, that is, choice of organic solvent with appropriate concentration of fluoride

ions and conductivity modifying additives—if so desired, as well as the anodization voltage range. The spacing between the nanotubes is found to vary with the type of organic solvent used. Speaking generally, ethylene glycol, for example, results in close-packed nanotube arrays [30], diethylene glycol enables broad control over the tube-to-tube spacing [31], dimethyl sulfoxide yields a two-layer structure where nanotubes are densely packed towards the substrate and well-separated nanotubes in the upper region [32], and the use of formamide results in well-separated nanotubes along the entire tube length [33, 34]. While fabrication of nanotube arrays on FTO-coated glass is not simplistic [35], TiO_2 nanotube arrays up to 53 μm in length have been achieved on FTO-coated glass.

As-anodized nanotubes are amorphous, crystallized by annealing in oxygen at elevated temperatures [36]. TiO_2 nanotubes arrays grown on FTO glass need to be annealed at relatively lower temperatures, no more than $\approx$470°C, to minimize damage to the FTO layer [35]. Annealing above this temperature promotes, we believe, diffusion of the residual Ti into the FTO layer and fluorine into the TiO_2 layer, with a corresponding loss in electrical conductivity. The walls of crystallized nanotubes are anatase, while any residual Ti layer underneath the nanotubes will convert to rutile [36].

Another approach to achieving self-assembled vertically oriented 1D TiO_2 nanostructured films, in this case nanowires, is by hydrothermal synthesis [25]. The self-assembled hydrothermally grown nanowires are of a highly crystalline rutile structure with preferred [001] orientation [25]. In comparison to rutile, use of anatase in DSSCs results in a higher photovoltage due to the higher conduction band level of anatase. Further, for equal degrees of crystallization, the charge transport properties of anatase are generally superior to those of rutile. Nanowire length is increased by the use of extended hydrothermal reaction times, but extended reaction times may also result in a thicker oxide layer at the nanowire base. Shorter nanowires have relatively wider wire-to-wire spacing; however, for a fixed wire length it is difficult to change the wire-to-wire spacing.

To date self-assembled 1D nanostructured titania films have yet to revolutionize third-generation photovoltaics; however, there remains hope that they yet may do so if synthesis techniques can be developed whereby single crystal films of such vertically oriented 1D structures, of extended length for enhanced light absorption, can be obtained without damage to the underlying transparent conductive layer to minimize series resistance. To that end, we consider herein our recent work on the synthesis of 1D nanostructured titania films and their photovoltaic application.

2. Fabrication of 1D Nanostructures

2.1. Transparent Films of TiO_2 Nanotube Arrays. As reported by Varghese and coworkers, there were three major challenges in the fabrication of transparent nanotube array films of extended length possessing high optical transparency and superior electrical properties as needed for application in achieving efficient dye-sensitized solar cells [35]. These were (i) formation of uniform titanium films tens of microns thick on FTO glass with sufficient adhesion to the FTO layer to withstand stresses associated with the anodization process and the different thermal and surface treatments inherent to DSSC fabrication; (ii) anodization of these thick titanium films until achieving uniform optical transparency; (iii) fabrication of TiO_2 nanotubes of great length using fluorine-containing nonaqueous organic anodization electrolytes without debris formation or clumping of the nanotubes [27].

Titanium films were deposited on FTO glass substrates, having sheet resistances of 15 Ω/square and 8 Ω/square, using radio frequency (RF) or direct current (DC) magnetron sputtering of titanium targets [35]. Film deposition was carried out at 5 mTorr in argon, with power densities of 6.34–7.92 W/cm^2 for RF and 4.3–5.66 W/cm^2 for DC sputtering. An RF source was connected to the substrate holder and negative DC self-bias voltages of 130 V and 160 V applied at the substrate for bombarding the growing films with positive argon ions for films of thickness below and above 2 μm, respectively. For films of thickness >3 μm, a second layer of thickness 0.5–0.8 μm was deposited across the top edge of the first layer, through use of a mask, to avoid complete etching of the film at the air-electrolyte interface during anodization. During deposition of the primary metal layer, the substrate was initially heated to about 45–60°C at which time the DC self-bias voltage was increased to about 210 V. No external heating was applied for depositing Ti films of thickness less than about 3 μm. Deposition rates up to 5.4 nm/minute were used. High optical reflectance (>55%) of the metal film was found to be a prerequisite for obtaining distinct-ordered nanotubes, indicating that the starting metal films should be dense and have a surface roughness limited to the nanometer regime.

TiO_2 nanotube arrays were formed by anodizing the Ti/FTO films, at constant voltage, in a two-electrode electrochemical cell with the titanium film as the anode and a platinum foil cathode. Dimethyl sulfoxide (DMSO) or ethylene glycol (EG) electrolytes containing with 2–4 vol% HF and 0–4 vol% water were used. Anodization was performed until the oxide nanotube growth fully consumed the titanium, across the entire thickness, and the film became transparent. The formation of debris, and increase in nanotube length beyond the metal film thickness in fluoride-based organic electrolytes is related to the low conductivity of the electrolyte. The conductivity of an electrolyte composed of hydrofluoric acid (HF) and DMSO, originally low, was enhanced by applying an electric field between two immersed electrodes (60 V between titanium and platinum electrodes). For obtaining debris-free short nanotubes, Ti anodization was done in an electrolyte of high electrical conductivity ($\sim$1000 μS/cm), whereas for longer nanotubes the electrolyte conductivity was low ($\sim$100 μS/cm). Voltages from 8 to 30 V (for the pore size 27 nm to 100 nm) were used for anodizing titanium films of thickness around 1 μm, whereas from 15 to 30 V were used for higher thickness Ti films for obtaining desired pore size and length. Anodization duration was 21–27 hours (at 30 V) for films comprising 20 μm long nanotubes. Transparent nanotube films from 0.3 μm to 33 μm in length were obtained from metal films of thickness up to

20 μm [35]. A field emission scanning electron microscope (FESEM) image of a TiO_2 film consisting of 20 μm long nanotubes is shown in Figure 1, reprinted with permission from [35]. The as-prepared films were annealed in an oxygen environment for crystallization, as well as for oxidizing any residual metal. The films were annealed in oxygen at temperatures ranging from 400°C to 530°C depending upon nanotube length; 1 μm thick films were annealed at 400°C for 6 h, and 20 μm films were kept at 400°C for 4 h and then at 530°C for 2 h. The high transmittance and low total reflectance of a 0.8 μm long nanotube film serves as an antireflection coating enhancing the transmittance by more than 5%, and decreasing the reflectance by about 6%. Even for a 17 μm thick nanotube film (on TEC 8), there is still significant transmittance in the red region. Prior to DSSC use, the films were immersed in 0.02 to 0.05 M $TiCl_4$ aqueous solution for 6–12 h, then rinsed with ethanol and distilled water, dried in air, and annealed at 450°C for 30 min in oxygen.

2.2. Transparent TiO_2 Nanowire Array Films. Feng et al. first reported the synthesis route for the fabrication of highly aligned, vertically oriented, densely packed, and highly crystalline nanowire arrays on FTO-coated glass [24]. The synthetic process was performed at relatively low temperatures, below 180°C, without affecting the FTO layer conductivity. Before growing the TiO_2 nanowire arrays, a compact TiO_2 layer 20 nm thick was grown by treating the FTO glass with 0.2 M $TiCl_4$ aqueous solution for 12 h and subsequently heating in air at 500°C for 30 min. These $TiCl_4$-treated FTO glasses were then placed within a sealed Teflon reactor (volume size ~23 mL) containing 10 mL of toluene, 1 mL of tetrabutyl titanate, 1 mL of 1.0 M titanium tetrachloride (in toluene), and 1 mL of hydrochloric acid (37 wt%) [24]. Nanowire array synthesis was achieved using toluene as the nonpolar solvent and toluene-soluble tetrabutyl titanate and titanium tetrachloride as a precursor. With an increase in temperature, Ti^{4+} precursors hydrolyze with water at the water/TiO_2 or FTO interface, resulting in the formation of a crystal nucleus on the substrate. After formation of the first nanocrystalline layer, a new interface forms between hydrophilic TiO_2 and toluene with continuous hydrolysis and subsequent growth-crystallization. A reaction temperature of 180°C was used with reaction times lasting from 30 min to 48 h. Nanowire growth was found to slow with time; for example, a 2 h reaction resulted in 2.1 μm long nanowires, a 4 h reaction leads to 3.2 μm long nanowires, 8 h to 3.8 μm, and 22 h to 4 μm; no increase in nanowire length was achieved for reaction times beyond 22 h. After the reaction period, the nanowire samples were removed, washed with ethanol, and then dried in air. The top and cross-sectional FESEM views of as-synthesized TiO_2 nanowire films, shown in Figures 2(a) and 2(b), reprinted with permission from [24], display a densely packed array of nanowires grown almost perpendicularly on FTO-glass. The nanowires were classified as tetragonal rutile with an enhanced (002) peak [24].

The interwire distance is a key parameter influencing the performance of hybrid photovoltaic cells. If the wires are too densely packed with small interwire separation, the bulky polymeric chains cannot percolate the full sample depth. At the same time, the nanowire separation should not be too great otherwise excitons generated in the interwire regions will recombine before being split at an available polymer-TiO_2 heterojunction. To form well-separated relatively short TiO_2 nanowire arrays, TiO_2 seed layer-coated FTO glass substrates were loaded into a sealed Teflon reactor (volume size ~23 mL) containing 10 mL toluene, 1 mL 1.0 M titanium tetrachloride (in toluene), 0.3 mL tetrabutyl titanate, and 1 mL hydrochloride acid (37 wt%), kept at 180°C for 8 h. Figures 2(c) and 2(d) show FE-SEM top and cross-sectional views of a typical as-synthesized nanowire array sample exhibiting vertically oriented nanowires of length ~600 nm, diameter ~15–35 nm, and interwire spacing ~30–50 nm. As per X-ray diffraction pattern analysis, these nanowires crystallized as tetragonal rutile with a preferred [001] crystal plane orientation.

3. Use of 1D Nanomaterials in Bulk Heterojunction, Ordered Heterojunction, and FRET-Type Solid and Liquid-Junction DSSCs

3.1. Bulk Heterojunction Solar Cell. Ideally the donor and acceptor phases within a bulk heterojunction are interspaced with an average length scale of around 10–20 nm, equal to or less than the exciton diffusion length, to ensure high mobility charge carrier transport with reduced recombination [39]. Such a precise nanostructure within polymer mixtures is difficult to achieve. However, self-organization of organic semiconducting polymers can be induced by use of diblock copolymers resulting in self-organized phases [40–42], liquid crystalline self-organizing columns of donor acceptor phases [43], and inorganic oxide nanotube or nanotemplate filled with organic semiconductors [38, 44–47]. Herein we emphasize the use of vertically oriented TiO_2 nanotube/nanowires for use with polymers as appropriate towards solid-state solar application.

Our initial design approach attempted to combine ordered 1D architectures for collecting electrons from PCBM molecules generated upon exciton dissociation at the P3HT/PCBM interface, and bulk heterojunctions present in a polymer/organic molecule blend [38]. A schematic of our device configuration is shown in Figure 3(a), with the highest occupied molecular orbital (HOMO) and lowest unoccupied molecular orbital (LUMO) energies of the component materials (P3HT/PCBM blend, PEDOT:PSS) with respect to the TiO_2 conduction and valence bands, and electrode (FTO and gold) work function, displayed in Figure 3(b). The length and pore size of TiO_2 nanotube arrays used were 270 nm and 50 nm, respectively. The polymer used was a blend of an electron donor P3HT and an electron acceptor $PC_{70}BM$; a 10 mg/mL solution of P3HT in chlorobenzene and 8 mg/mL solution of PCBM in chlorobenzene were mixed in a 1 : 1 ratio using the procedure outlined by Kim et al. [48] and infiltrated into the nanotubes. Subsequently, a PEDOT:PSS layer was deposited by spin coating an aqueous suspension of the polymer at 5000 rpm. The samples were then placed

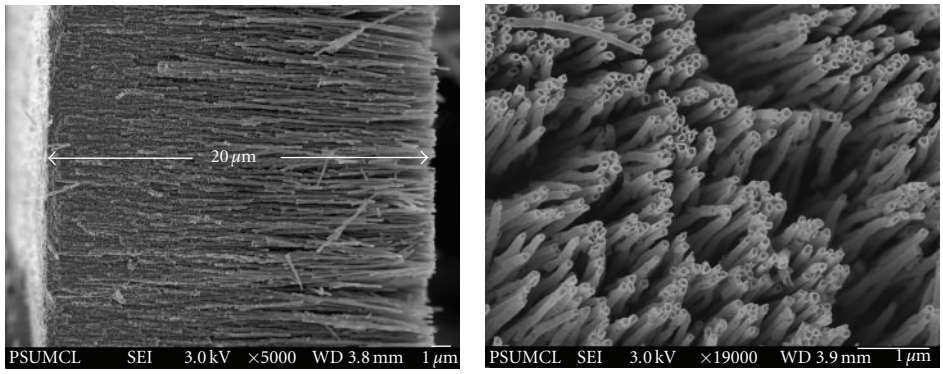

(a) (b)

Figure 1: (a) FESEM image of a 20 μm long TiO_2 nanotube array (pore size 95 nm and wall thickness ~10 nm) on FTO-coated glass and (b) top view of the nanotubes. Reprinted with permission from [35].

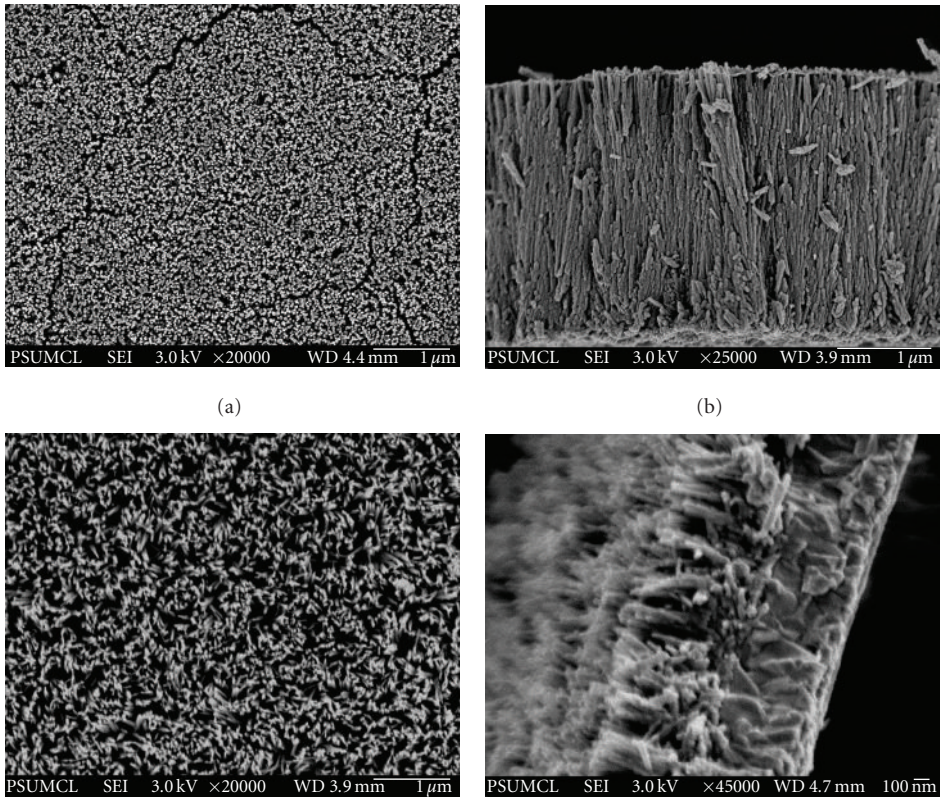

(a) (b)

(c) (d)

Figure 2: (a) Top and (b) cross-sectional FESEM images of vertically oriented self-organized rutile TiO_2 nanowire array grown on FTO coated glass at 180°C for 24 h. Reprinted with permission from [24]. (c) Top-view and (d) cross-sectional FESEM image of short rutile TiO_2 nanowire arrays.

on a hot plate at 170°C for 15 min to remove any residual water and to promote intercalation of the polymer into the TiO_2 nanotube arrays. All spin coating and baking steps were carried out in a nitrogen glove box. A 50 nm film of gold was evaporated onto the devices though a shadow mask to form the top contact.

Charge separation occurs at the TiO_2/P3HT and PCBM/P3HT interfaces. The barrier layer of compact TiO_2 prevents holes in the polymer from reaching the transparent conductive oxide. A key advantage of the TiO_2 nanotube array electron-accepting network is that it prevents the electron-donating material (P3HT) and electron-accepting materials (TiO_2 and PCBM) from both being in contact with anode and cathode of the solar cell at the same time, as is the case with the conventional bulk heterojunction device geometry. The J-V characteristics of the fabricated TiO_2

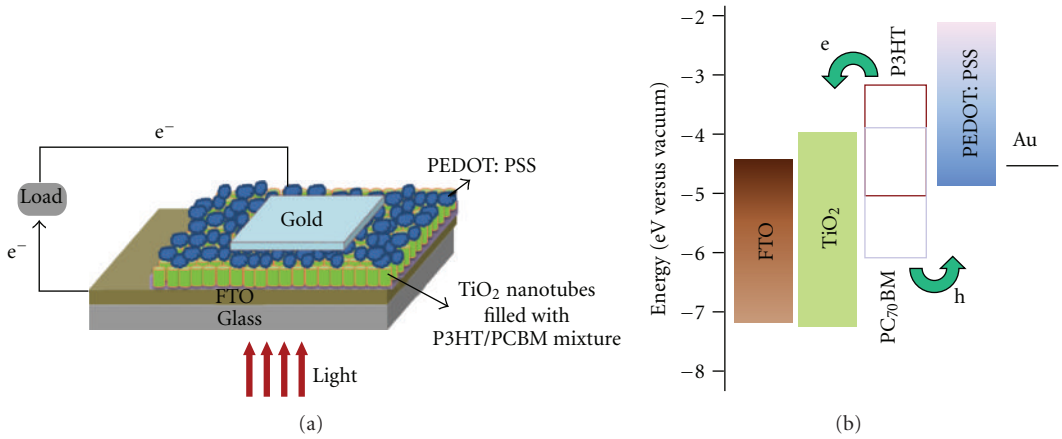

FIGURE 3: (a) Schematic device configuration of polymer TiO_2 nanotube-array-based solid-state solar cell, (b) HOMO and LUMO energies of the component materials of polymer TiO_2 nanotube-array-based solar cell. Reprinted with permission from [37].

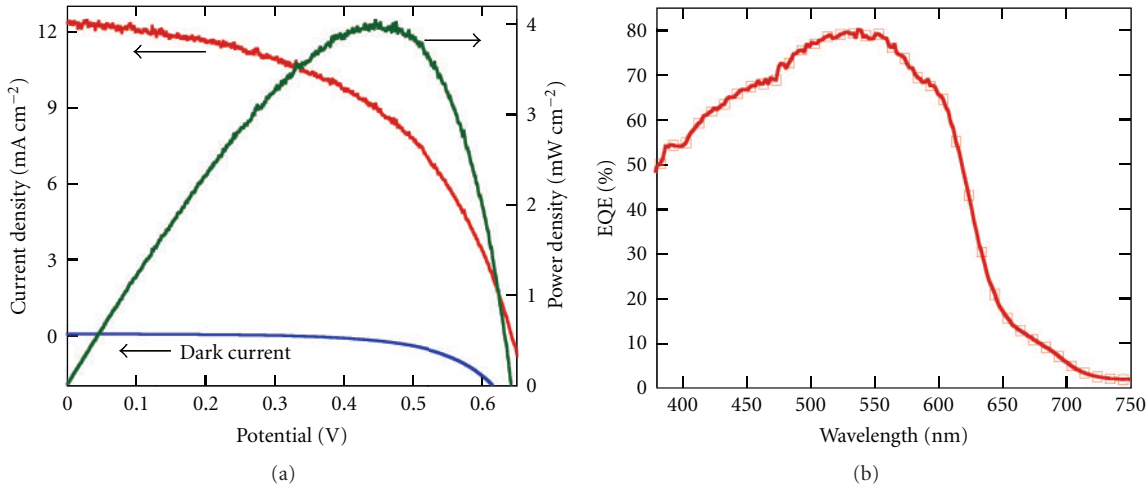

FIGURE 4: (a) *J-V* characteristics of TiO_2 nanotube array-polymer bulk heterojunction solar cells showing the dark current, photocurrent, and power density under 1 sun AM 1.5 illumination. (b) EQE of the nanotube array-polymer bulk heterojunction solar cells. Reprinted with permission from [38].

nanotube array-polymer solar cells under AM 1.5 global illumination are shown in Figure 4(a). The short circuit density is 12.43 mA/cm^2, the open circuit potential was 641 mV, and the fill factor was 0.511, resulting in an overall conversion efficiency of 4.07%. We surmise that the coiling of the polymer chains inside the nanotube pores, as manifested by the blue shift in the absorption peak relative to the neat unannealed film, may be responsible for relatively poor hole transport thus negatively impacting the fill factor. Figure 4(b) shows the external quantum efficiency (EQE) plot of the nanotube array-polymer double heterojunction solar cells, with a maximum value of 80% seen at 538 nm. When adjusted for photonic losses, which include an approximate 15% absorption loss due to the FTO coating and glass substrate, the reflection losses at the FTO-TiO_2 interface, and the FTO-glass interface, the conversion of incident photons at the absorption peak wavelength into collected electrons is nearly quantitative. The position of the EQE maximum at 538 nm is different from conventional bulk heterojunction cells where it occurs close to 500 nm [49], a difference we believe due to the device geometry and stacking order of the absorbing layers.

An alternative device configuration investigated was FTO/TiO_2 nanotubes/P3HT-PCBM/PEDOT:PSS/gold, with illumination through the FTO-glass substrate. The conduction band position of TiO_2 is just below the LUMO energy level of PCBM, resulting in efficient extraction of electrons from the PCBM. The nanotube architecture enhances the interfacial contact area between TiO_2 and P3HT and/or PCBM of the active blend layer, which implies a higher electron collecting surface area. The length of the nanotubes used was 600–700 nm with a pore size of 35 to 40 nm. P3HT and $PC_{70}BM$ blends prepared in chlorobenzene are less polar in nature and do not readily wet the TiO_2 surface which is hydrophilic in nature. For making a blend solution, we replaced chlorobenzene (CB) by o-dichlorobenzene

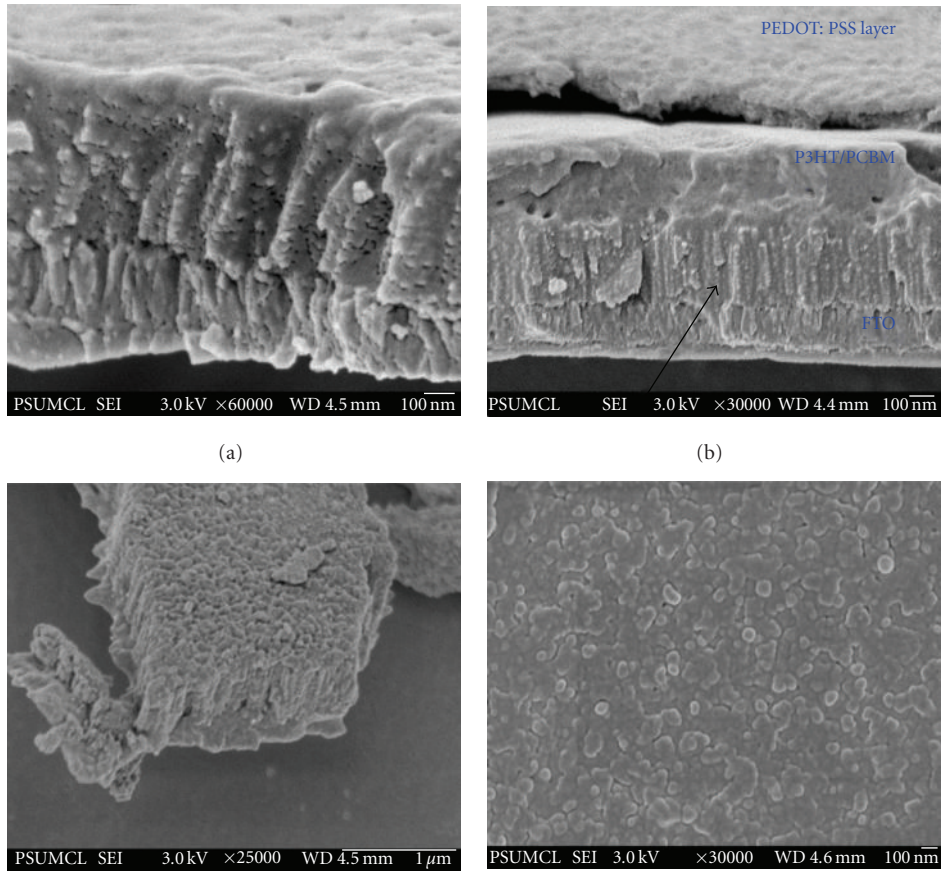

Figure 5: FESEM cross-sectional view of (a) P3HT/PCBM blend-filled nanotubes; (b) full device, with arrow denoting layer of P3HT/PCBM blend-filled nanotubes, with PEDOT:PSS layer on top. (c) FESEM cross-sectional view, of mechanically fractured sample, showing polymer blend decorated nanotubes with top unblocked. (d) Top view of PEDOT:PSS-coated full device. Reprinted with permission from [37].

(o-DCB), which is relatively more polar. The solubility of $PC_{70}BM$ in O-DCB is quite high, about 70 mg/mL, whereas chlorobenzene can dissolve only approximately 40 mg/mL of $PC_{70}BM$. To infiltrate the polymer inside the nanotubes, we wet the nanotube surface with O-DCB and then spin the nanotube sample such that the nanotubes are filled with solvent, while the excess solvent is driven away from the nanotube surface. Here the nanotube dimensions, concentration of the blended solution, and the spin speed are critical variables and require rigorous process optimization. When the P3HT/$PC_{70}BM$ samples are removed from the spin coater, they should be wet. Subsequent baking of the wet samples on hot plate at 150°C further assists the diffusion of the polymer blend into the nanotubes.

Crystallized nanotube array samples were wet with o-DCB, and the excess-solvent spun from the surface. Then a drop of P3HT + $PC_{70}BM$ (conc.) was placed on the wet surface. P3HT/$PC_{70}BM$ was mixed in ratio of 1 : 0.8 and dissolved in DCB : CB organic-solvent mixture (from 2 : 1 to 4 : 1 and then from 1 : 2 to 1 : 4). The sample was then spun, slowly ramping to a final spin speed of 300 rpm. Subsequent baking of the wet sample was performed in closed petri dish covered with aluminum foil at 150°C for 30 mins, after which it was allowed to cool at room temperature on a metal plate for 0.5 h. Afterward, a PEDOT:PSS layer was spin-coated from aqueous solution at 4000 rpm for 120 s, and then baked at 120°C for 8–10 mins in a covered petri dish. The sample was allowed to cool at room temperature for 15 min before taking the sample from the glove box for DC sputter coating of Au circular pads through a mask. Figure 5(a) shows the TiO_2 nanotube walls decorated with polymer and the opening of the tube covered with polymer. Figure 5(b) shows the cross-sectional view of the full device covered with a PEDOT:PSS layer. Figures 5(c) and 5(d) illustrate another device showing the polymer-decorated nanotubes with top unblocked for PEDOT:PSS layer infiltration. Current-voltage characteristics and the overall conversion efficiency of the photovoltaic devices made using P3HT/PCBM-coated TiO_2 nanotubes are shown in Figure 6(a), with corresponding efficiencies shown in Figure 6(b). There are five curves in the I-V plot, each curve represents the treating/wetting of nanotubes with different type of organic solvents just before putting a concentrated P3HT/PCBM solution. Curve 1 represents the device performance of nanotubes treated with t-butyl pyridine (TBP). TBP is a polar solvent, which can easily wet the hydrophilic surface of nanotubes but

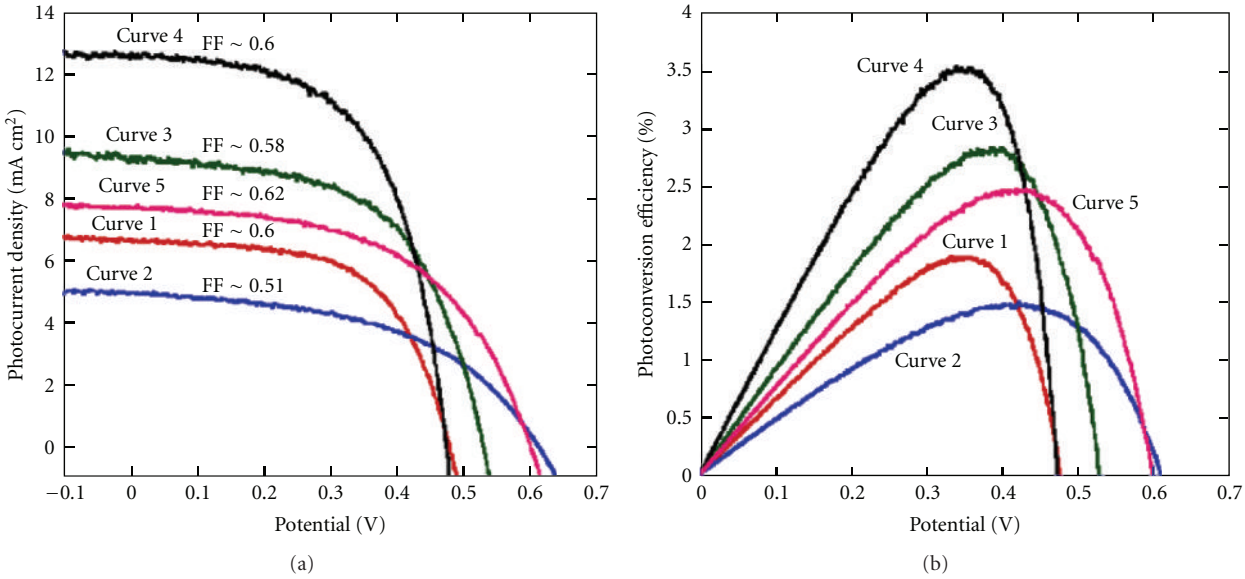

Figure 6: (a) Current-voltage characteristics and (b) the overall conversion efficiency of solid-state photovoltaic devices made using P3HT/PCBM-coated TiO_2 nanotubes. Five curves, 1 to 5, represent five different TiO_2 surface treatments before polymer blend spin coating. Treatment of nanotubes for (1) Curve 1—TBP, (2) Curve 2—CB, (3) Curve 3—o-DCB, (4) Curve 4—soaked in o-DCB, and (5) Curve 5—soaked in o-DCB and baked at 165°C. Curves 1 to 4 were baked at 150°C. Reprinted with permission from [37].

does not allow the polymer film to penetrate within the nanotube pores; minimal polymer coverage of the nanotubes leads to small current. Replacing TBP with chlorobenzene (CB), we achieved the device performance displayed by curve 2. Though the photocurrent is low, the photovoltage is close to the expected value obtained in a conventional bulk heterojunction device. Treating the TiO_2 surface with o-DCB, which has polarity higher than that of CB but lower than TBP, we achieve higher saturated photocurrent density, as shown by curve 3, with a photovoltage higher than that achieved in the TBP-treated sample but lower than that of the CB-treated surfaces. Thoroughly wetting the nanotubes with o-DCB improved the polymer intercalation, with the performance of such a photovoltaic device illustrated by curve 4. All devices shown by curves 1 to 4 were baked at 150°C for 30 min after spin coating on the polymer solution. Using a higher baking temperature of 165°C on our best device, curve 4, resulted in a 4 mA/cm^2 drop in photocurrent but an increase in photovoltage to 0.61 V, see curve 5. Curve 4 showed the best photoconversion efficiency of ≈3.5%, with the low voltage apparently due to high dark currents. Choice of solvent, and its ability to prevent water molecules from residing at the inorganic-organic interface, plays a critical role in determining the overall efficiency of the photovoltaic devices. Two kinds of photovoltaic devices were fabricated by infiltrating organic semiconductors into rutile nanowire arrays, see Figure 2(d), with the first being a blend of P3HT and PCBM and the second purely P3HT. The polymer blend solution prepared in chlorobenzene contained 10 mg/mL of P3HT and 8 mg/mL of PCBM, the optimized concentrations as suggested by Kim et al. [48]. For both kinds of devices, the device fabrication process was identical: the TiO_2 nanowire array sample was wetted with the polymer solution for 30 s, and then spin coated at 600 rpm. The sample was then baked at 150°C for 10 min in a covered petri dish and finally cooled to room temperature. Subsequently, a layer of hole injecting PEDOT:PSS was deposited by spin coating an aqueous suspension of the polymer at 4000 rpm. The samples were then placed on a hot plate at 120°C for 10 min. All spin coating and baking steps were carried out in an inert ambient glove box. Finally a 50 nm film of gold was evaporated onto the devices through a shadow mask to form the back contact (rectangular size—2.2 × 3.4 mm^2). The average length of the TiO_2 nanowire array and the total thickness of the active layer were 600 and about 700 nm, respectively. Outside the gold top contact area, the PEDOT:PSS layer was carefully scrapped away to avoid any photocurrent contribution from that region. The solar cell testing was performed in air.

A photocurrent density-potential (J-V) characteristic of a typical TiO_2 nanowire array-P3HT and PCBM polymer blend solar cell under AM 1.5 global illumination from a calibrated Class A solar simulator is shown in Figure 7(a). The short circuit current density (J_{sc}) is 8.3 mA/cm^2, the open circuit potential (V_{oc}) 0.44 V, and the fill factor 0.41, resulting in an overall conversion efficiency of 1.5%. In Figure 7(b), the incident photon to current conversion efficiency (IPCE) of the device is plotted as a function of wavelength. The maximum IPCE value for the TiO_2 nanowire device reaches about 56% at 550 nm. Upon integrating the current irradiance, determined using the IPCE curve over the wavelength range from 350 to 750 nm, the value of the overlap integral is close to the J_{sc} obtained from the J-V plot. The electrical characteristics of a typical photovoltaic cell using pure P3HT, not shown, without addition of PCBM were also investigated; for this type of cell, the nanowire array was first coated with a monolayer

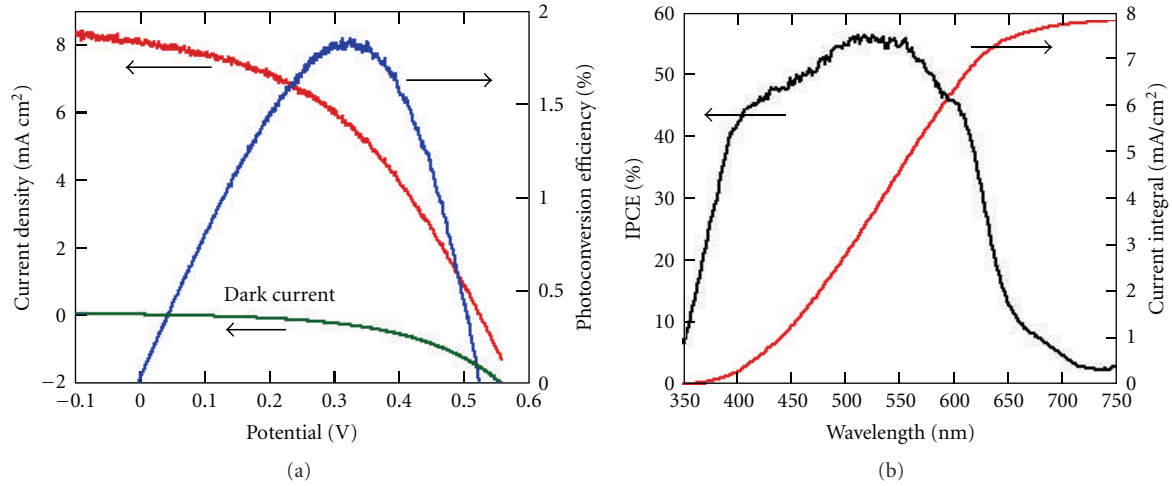

FIGURE 7: J-V characteristics and photoconversion efficiency of TiO_2 nanowire array-polymer blend (P3HT:PCBM) heterojunction solar cell. (b) The IPCE and overlap integral of photocurrent irradiance of the described TiO_2 nanowire array-polymer heterojunction solar cells. Reprinted with permission from [37].

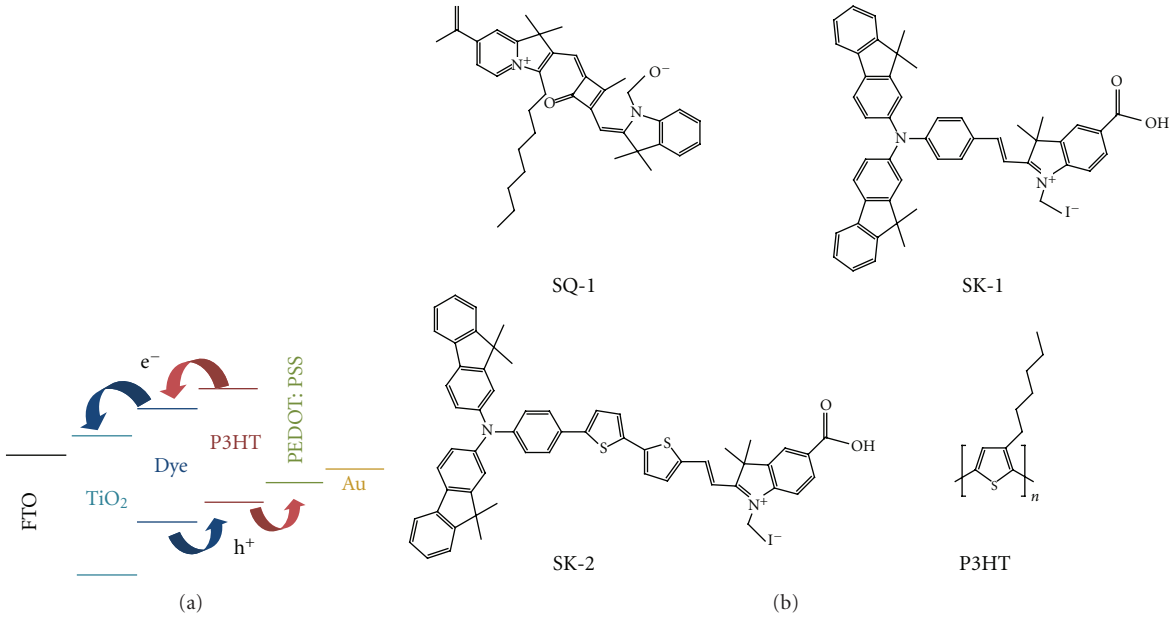

FIGURE 8: (a) Depiction of energy level positions and charge transfer processes of the constituent layers of the described hybrid solar cell. (b) Molecular structure of organic dyes (SK-1, SK-2, SQ-1) and P3HT polymer. Reprinted with permission from [7, 51].

of N-719 dye by immersion in a 0.5 mM ethanol solution of dye overnight to suppress recombination. J_{sc} is 1.5 mA/cm^2, V_{oc} 0.56 V, and the fill factor 0.55, resulting in an overall conversion efficiency of 0.46%. For charge transfer to occur efficiently between the regioregular P3HT and the TiO_2, a TiO_2-P3HT interface needs to be within 10–20 nm of every produced exciton [50]. However, an average nanowire separation of 30 nm existed in our samples; consequently, a significant fraction of the excitons generated in the P3HT are lost to recombination resulting in a lower photocurrent. When a blend of P3HT and PCBM is used, two interfaces, namely, the TiO_2-P3HT and the PCBM-P3HT interface, are available for exciton splitting. Therefore, charge separation is improved and the photocurrent densities are higher in devices employing the blend.

3.2. Ordered Heterojunction Solar Cell. We consider a heterojunction solar cell where unsymmetrical squaraine (SQ-1) organic dye decorated vertically oriented nanotubes are infiltrated with P3HT [7]. The HOMO-LUMO levels favor electron injection from P3HT into the dye and then to the TiO_2, see Figure 8(a). We also investigated two other hemicyanine organic dyes, SK-1 and SK-2 [51], as shown in Figure 8(b), having different optical and electrochemical properties to modify the TiO_2 interface and compared their solar cell performance with respect to SQ-1 dye as a

Table 1: Absorption, emission, and electrochemical properties of SQ-1, SK-1, SK-2 dyes, and P3HT polymer [7, 51].

Dye/Polymer	λ_{abs}[a], nm (ε, $M^{-1}cm^{-1}$)	λ_{em}[a], nm	E_{ox}[b]/[V versus Fc/Fc$^+$]	$E_{0\text{-}0}$[c], [eV]	E_{HOMO}[d], [eV]	E_{LUMO}[d], [eV]
SK-1	342, 582	642	0.41	2.00	5.21	3.21
SK-2	359, 619	721	0.63	1.85	5.43	3.58
SQ-1 dye	637 (159, 700)	652	0.38	1.93	5.18	3.25
P3HT	443	568	—	1.9	5.1	3.2

[a]Absorption and emission spectra were measured in ethanol solution.
[b]A silver wire was used as a pseudoreference electrode and was calibrated with a ferrocene/ferrocenium (Fc/Fc^+) redox couple. The electrochemical experiments were measured in CH_3CN with 0.1 M $(n\text{-}C_4H_9)_4NPF_6$ with a scan rate of 100 mVs^{-1}.
[c]$E_{0\text{-}0}$ was determined from intersection of absorption and emission spectra in ethanol.
[d]The energy levels of the HOMO and LUMO were determined using the following equations: E_{HOMO} (eV) = $E_{ox} - E_{FC/FC^+} + 4.8$ eV and E_{LUMO} (eV) = $E_{HOMO} - E_{0\text{-}0}$.

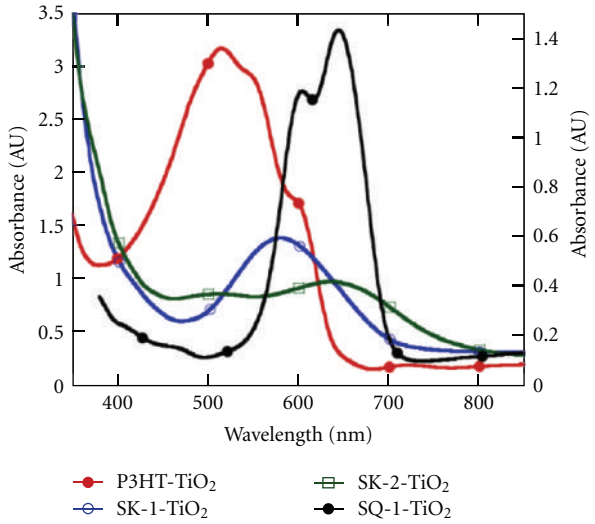

Figure 9: Optical absorbance of SK-1-, SK-2-, and SQ-1-sensitized TiO_2 nanotube arrays, and P3HT intercalated nanotube arrays without dye sensitization. The nanotube arrays had an average pore size of 35 nm and tube length of 600–700 nm. Reprinted with permission from [7, 51].

sensitizer. As seen in Figure 8(b), the molecular structures of the SK dyes have different π-conjugation lengths between the bis-dimethylfluoreneaniline moiety acting as electron donor and carboxylic acid moiety acting as electron acceptor. These two parts are connected by a 1-ethyl-3,3-dimethyl-3 *H*-indolium moiety.

Figure 9 displays the UV-Vis-NIR absorption spectra of four samples, TiO_2 nanotube arrays sensitized with SK-1, SK-2, or SQ-1 dyes, and P3HT-infiltrated TiO_2 nanotube array films [7, 51]. P3HT coverage of the TiO_2 nanotube arrays shows no shift in the absorption peak position compared to that of neat P3HT films [52], indicating a high degree of π-π stacking of the polymer chains within the nanotubes. Compared to the organic dyes, P3HT is highly absorbing in the visible range. The absorption spectrum of the dyes on the nanotube array films is broadened due to interaction between dye and TiO_2 [53]. Dye sensitization of nanotube arrays with SK-2 dye results in a red shift in the absorption peak, while no such change was observed for the SK-1 dye. The absorption spectra of SQ-1 on the TiO_2 nanotubes arrays films show a small red shift of 9 nm suggesting J-type aggregation, which can further extend the photon absorption into the NIR region. The LUMO levels of the two dyes adsorbed on the TiO_2 nanotube array films, estimated from the oxidation potentials and the excitation transition energy ($E_{0\text{-}0}$) determined from the intersection of absorption and emission spectra, are listed in Table 1. The excitation transition energy ($E_{0\text{-}0}$) of SK-1 and SK-2 are calculated to be 2.00 and 1.85 eV, respectively. The reduced excitation transition energy of SK-2 is due to extension of the π-π conjugation length associated with the two additional thiophene units. The LUMO level of the dyes (SK-1: 3.21 eV and SK-2: 3.58 eV) is much higher than the TiO_2 conduction band, suggesting that electron transfer from the excited dye to the TiO_2 conduction band is readily feasible. The LUMO level of the SQ-1 dye is more negative than the P3HT LUMO level and less negative than the TiO_2 conduction band, while the HOMO level of the SQ-1 dye is close to or slightly below the HOMO level of P3HT. Hence, upon absorption of a red/NIR photon, the organic dye injects an electron into the TiO_2 conduction band and is regenerated by donation of a hole to the P3HT.

First, we consider the use of SQ-1 dye as a sensitizer which absorbs in the red and NIR portion of solar spectrum in combination with hole conducting P3HT that absorbs higher energy photons. The low band gap organic dye does not block transmission of the high-energy photons of near UV-visible range, see Figure 9 [7]. In our device, excited states generated in the dye find themselves in close proximity to two interfaces for dissociation: the TiO_2-dye interface and the dye-P3HT interface. For excitons generated in the P3HT, the P3HT-dye interface is the closest available for splitting, and the largest distance the excitons need to diffuse to reach this interface corresponds to the radius of the nanotube pore. After exciton splitting, electrons are injected into the TiO_2, while hole-polarons travel through the P3HT layer to the PEDOT:PSS hole collection contact. The open circuit voltage V_{oc} is determined by the TiO_2 quasi-Fermi level and the P3HT HOMO level. The TiO_2 nanotube array pore size, from 20 to 35 nm, was selected such that P3HT chains can infiltrate into the pores but also allow photogenerated excitons in the P3HT to readily diffuse to

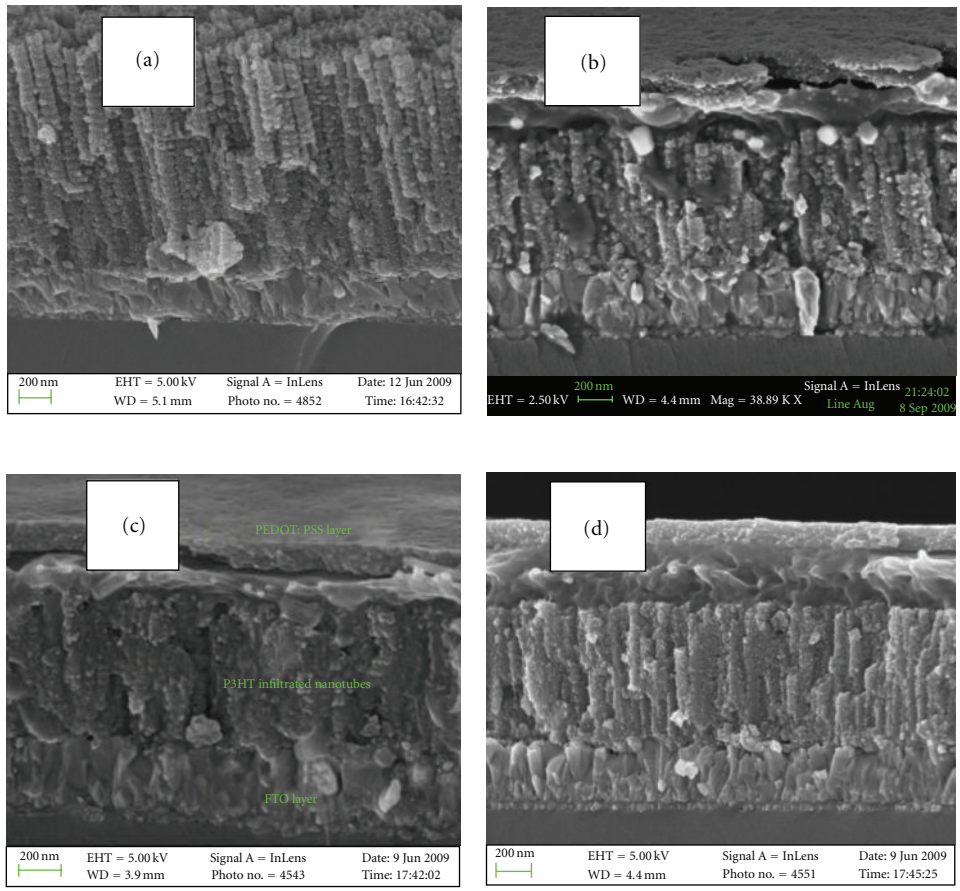

FIGURE 10: (a) Typical cross-sectional view of 60 nm pore size, 1–1.2 μm length TiO_2 nanotube array film after $TiCl_4$ treatment. Cross-sectional FESEM image of TiO_2 nanotube (≈35 nm pore size, ≈600–700 nm nanotube length)/SQ-1 dye/P3HT/PEDOT:PSS photovoltaic devices showing: (b) nanotubes partially infiltrated with polymer, fabricated under the condition of excess wetness; (c) fully infiltrated nanotubes fabricated under optimized wetness condition; and (d) partial infiltration of the P3HT polymer within the nanotubes, fabricated under dry condition. Reprinted with permission from [7].

the exciton splitting interface. This configuration has the following key advantages [7]. (i) The ordered heterojunction architecture provides percolation paths for both types of charge carriers. (ii) The vertically oriented nanotube array architecture decouples exciton diffusion from light absorption. (iii) There are two complementary photon absorbers that provide broad-spectrum absorption, namely, the dye molecules anchored to the nanotube walls and the organic semiconductor (P3HT) within the nanotubes.

Devices built upon nanotube arrays having three different average pore sizes, namely, 20 nm (length ~500 nm), 35 nm (length ~600 to 700 nm), and 60 nm (length ~1 to 1.2 μm) were investigated [35]. All samples were crystallized and treated with aqueous $TiCl_4$ solution under identical conditions. A cross-sectional FESEM view of a $TiCl_4$-treated nanotube array film (length ~1 to 1.2 μm) is shown in Figure 10(a). The nanotubes have the general shape of a common laboratory test tube, with the top of the tube open and the bottom closed [37, 54]. To assist polymer infiltration within the tubes, the nanotube array film was wetted with p-xylene, a nonpolar organic solvent. After removing the excess solvent, nanotube arrays were covered with a P3HT polymer solution (30 mg/mL concentration) prepared in a 3 : 1 mixture of ortho-dichlorobenzene (o-DCB) and chlorobenzene (CB). The sample was then spun, with the p-xylene acting to wick the P3HT inside the nanotube arrays and the polymer solution forming a thin layer atop the nanotube array film. The sample was then immediately transferred onto a hot plate, with the remaining organic solvent quickly evaporating and the polymer inside the nanotubes making a dry interface with the dye molecule layer. Previously, Coakley and coworkers had demonstrated the infiltration of P3HT into the pores of alumina/titania using a polymer melt-infiltration technique [55]. After cooling the sample to room temperature, a thin layer of PEDOT:PSS was spun onto the sample. It was then baked at 120°C to remove water present in the PEDOT:PSS layer, avoiding degradation of the P3HT, and then finally at 150°C to promote adhesion between the PEDOT:PSS and P3HT layers.

The duration of the spin-coating to control the wetting of P3HT solution upon the dye-sensitized TiO_2 nanotube arrays depends on the following factors: type of glove box,

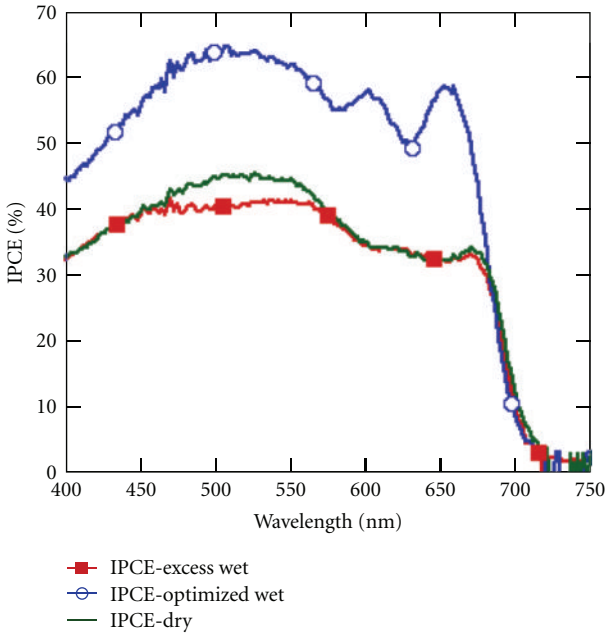

Figure 11: IPCE of an FTO/TiO_2 nanotube array/SQ-1 dye/P3HT/PEDOT:PSS/Au solar cell, where the P3HT layer was prepared with different degrees of surface wetness prior to a 150°C postbake. Excess wetness, where the film was still wet entering the postbake; dry, indicating where the film had dried on the spinner prior to postbake; optimized, where upon just visually drying the device was immediately removed from the spinner and exposed to the postbake. The dye sensitization and PEDOT:PSS layer are identical in all the three samples. Nanotube array films of 35 nm average pore diameter and 600–700 nm length were used. Reprinted with permission from [7].

air circulation, and what the inert gas pressure is inside the glovebox when the device is fabricated. Hence instead of specifying the exact spinning duration, we instead describe the sample condition. After performing the suggested initial treatment with p-xylene on dye-sensitized TiO_2 nanotube arrays, the sample surface was completely covered with P3HT solution (30 mg/mL, prepared using a 3 : 1 ratio of o-DCB and CB) and then spun at 250 rpm. Spinning the sample for 200–300 s, a wet layer of excess P3HT on top of nanotube arrays was observed. This sample was immediately transferred to a hot plate and baked at 150°C for 20 minutes which resulted in partial infiltration of the polymer inside the nanotubes due to evaporation of the o-DCB solvent. A cross-sectional image of this sample with a PEDOT:PSS layer deposited on top is shown in Figure 10(b). On further extending the spinning time to 350–400 s, the P3HT film was partially wet (optimized wet). Immediately baking the sample on a hot plate resulted in complete filling of the tubes, see Figure 10(c). Extended spinning durations, that is, 450 to 500 s, resulted in a dry P3HT layer from which only partial decoration of the nanotube walls was achieved, see Figure 10(d). The glancing angle X-ray diffraction (GAXRD) pattern of the completed device showed the presence of highly crystalline P3HT, where the peak at $2\theta = 5°$ corresponds to a P3HT interchain spacing associated with interdigitated alkyl chains [56, 57].

Details of the device structure, and hence performance, are dependent on the device fabrication procedure. Consider as an illustration the IPCE of three of the described P3HT/dye-sensitized TiO_2 nanotube array devices, see Figure 11, with the P3HT solution (30 mg/mL, prepared using a 3 : 1 ratio of o-DCB and CB) applied in varying degrees of sample surface wetting. Samples coated with an excess amount of P3HT solution, where spinning is stopped before the P3HT solution dries, had minimal polymer within the tubes presumably due to evaporation of the o-DCB solvent. Cells fabricated with a minimal amount of P3HT solution, that is, spinning was stopped after the P3HT solution had completely dried, had only partial decoration of the P3HT on the nanotube walls. Optimal device performance was achieved with an intermediate surface wetting, with the sample removed from the spinner just before the polymer dried, then immediately transferred to the 150°C hot plate. This timing of surface wetting/drying resulted in full penetration of the polymer into the nanotubes, with the polymer making uniform contact with the organic dye layer. Such samples exhibit an IPCE of 50–65% between 420 and 680 nm. The resulting samples appear reddish with a light violet tinge. Due to significant overlap between the emission spectrum of P3HT and the absorption spectrum of the SQ-1 dye, exciton transfer from P3HT to the dye by Förster-type resonance energy transfer (FRET) is possible [9, 58–62]. Upon calculating the spectral overlap integral from the normalized photoluminescence (of P3HT on a very thin TiO_2 film) [59] and absorption (of SQ-1 dye ethanolic solution) spectra, considering an emission quantum efficiency of 1% for P3HT [60], and assuming random orientation of the donor and acceptor molecules and the effective refractive index of P3HT-TiO_2 film of 1.6, we calculate a Förster radius [58] of 2.58 nm which could result in an effective exciton diffusion length in the range of 14 to 18 nm [61, 62]. Based on the exciton harvesting calculation given by Scully and coworkers [62], it was found that about 65–75% of the excitons generated in P3HT infiltrated inside 35 nm pore size TiO_2 nanotube arrays can be harvested. The coexistence of resonance energy transfer may account for the high charge transfer efficiencies in this system as inferred from external quantum yield measurements.

The fill factor and open-circuit voltage of the SQ-1 dye-based solar cells was further improved by wetting the SQ-1 sensitized nanotube array films (pore size ~35 nm, tube length 600–700 nm) with 0.05 to 0.1 M tert-butyl pyridine in p-xylene solution (instead of pure p-xylene), spin coating the P3HT and PEDOT:PSS layers, depositing the gold electrode, and then baking the device at 120°C for 1 min in air. The performance of a typical device is shown in Figure 12, with $J_{sc} = 10.75\ \text{mA/cm}^2$, $V_{oc} = 0.55$ V, FF = 0.55, and $\eta = 3.2\%$. Tert-butylpyridine is known to increase the open circuit voltage by upwards shifting the TiO_2 band edge [63, 64], and by physically sealing molecular scale voids at the interface. The efficiency of our champion device was found to be 3.8% ($J_{sc} = 11\ \text{mA/cm}^2$, $V_{oc} = 0.6$ V, FF = 0.58). If we account for the transmittance loss of 10% across the visible range due

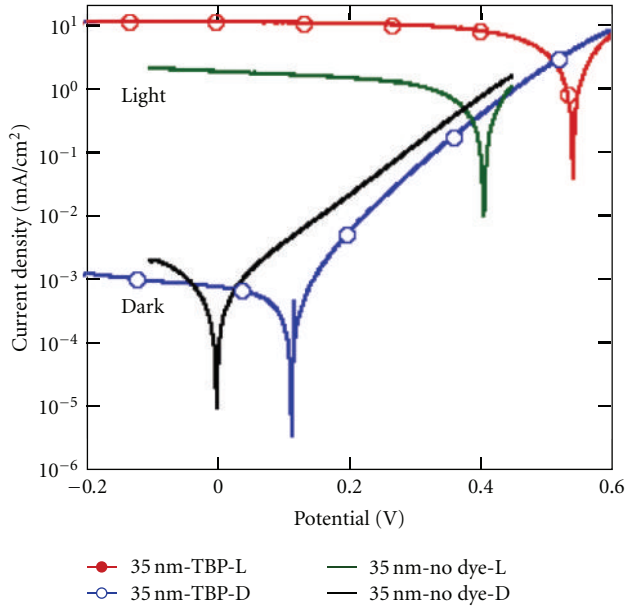

FIGURE 12: J-V curves showing the improved performance of a FTO/35 nm pore, 600–700 nm length TiO_2nanotube array/SQ-1 dye/P3HT/PEDOT:PSS/Au hybrid solar cell where the dye-sensitized nanotube array surface, prior to application of the P3HT layer, is wetted with 0.05 to 0.1 M tert-butyl pyridine in p-xylene. Also shown is the performance of an otherwise identical cell lacking the SQ-1 dye layer. L denotes cell performance under light illumination D denotes cell performance in the dark. Reprinted with permission from [7].

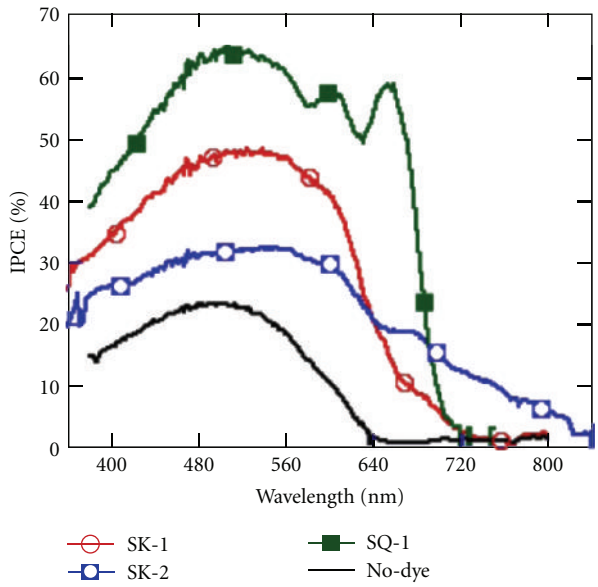

FIGURE 13: IPCE spectra of four hybrid solar cell device structures, namely, FTO/TiO_2 nanotube array/SK-1, SK-2, SQ-1, or no dye layer/P3HT/PEDOT:PSS/Au. The dye sensitization and PEDOT:PSS layer are identical in the four samples. Reprinted with permission from [51].

to the UV filter in the light source (necessary since UV light rapidly degrades the SQ-1 dye), an efficiency of ≈4.2% can be expected. The performance of a TiO_2 nanotube array/P3HT solar cell without an organic dye layer is also shown in Figure 12; $J_{sc} = 1.8$ mA/cm^2, $V_{oc} = 0.41$ V, FF = 0.46, and $\eta = 0.34\%$.

With use of the organic dye layer, the photoconversion efficiency of a typical device increases from 0.34% to 3.2%, with the open circuit voltage increasing from 0.41 V to 0.55 V. Acid-base interactions arising from carboxylic group anchoring of the organic dye affect the TiO_2 band edge by protonating it. As reported by Goh and coworkers [65], the magnitude of this shift is about 0.2 eV for Ru (II) dyes. It was also noted that extensive $TiCl_4$ treatment of the nanotubes was found to increase the open-circuit voltage to 0.67 V, but resulted in considerably lower photocurrents. The J-V and IPCE measurements of our devices were performed in air and the photovoltaic results were consistent for a number of runs made on several days.

Figure 13 shows the IPCE of four hybrid solar cell device structures, namely, FTO/TiO_2 nanotube array/SK-1, SK-2, SQ-1, or no dye layer/P3HT/PEDOT:PSS/Au [51]. The hybrid cell without an organic dye layer shows a maximum IPCE of 22% between 350 and 650 nm; it appears that these relatively small IPCE values are due to the poor interface between the organic polymer and inorganic oxide. The increase in the photocurrent action spectrum for wavelengths beyond 650 nm is due to charge injection from the dyes. In the SK-1 solar cell, IPCE values improve to 50% in the visible range with photocurrent generation up to 750 nm. The photoaction spectrum closely matches the optical absorption spectrum of the SK-1 dye and P3HT polymer, confirming that the observed photocurrent arises from electron injection by the SK-1 dye and P3HT polymer. The IPCE values of the SK-1 device are comparatively small in the red and NIR region due to the relatively lower absorption coefficient of SK-1 dye in this range. With the SK-2 dye, we observe relatively lower values of IPCE in the visible range, a maximum value of about 30%; however, significant IPCE values extend up to 800 nm. In the SQ-1 solar cells, an IPCE of 50–65% is achieved between 420 and 680 nm, indicating that these high IPCE values are at least partially due to the smaller absorption overlap with that of the P3HT polymer. That is, two complementary photon absorbers can provide broad-spectrum absorption.

Regarding the J-V characteristics of FTO/TiO_2 nanotubes/SK-1 or SK-2/P3HT/PEDOT:PSS/Au hybrid solar cells [51], we found that the photovoltaic performance of a typical SK-1 cell are $J_{sc} = 6.7$ mA/cm^2, $V_{oc} = 0.56$ V, FF = 0.43, and $\eta = 1.61\%$. The photovoltaic properties of a typical SK-2 cell are $J_{sc} = 5$ mA/cm^2, $V_{oc} = 0.6$ V, FF = 0.52, and $\eta = 1.57\%$. Our champion SK-dye-based devices demonstrate photoconversion efficiencies of ≈1.9%. It is clear that the dye layer upon the TiO_2 nanotube array substrate acts both as a photo-sensitizer and electronic mediator, significantly improving both the photocurrent and the photovoltage of the solar cell.

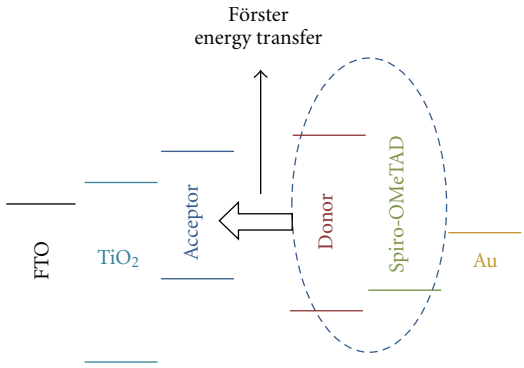

Figure 14: Depiction of energy level positions of FRET-type solid-state dye-sensitized solar cell (SS-DSSC) constituents. Reprinted with permission from [12].

3.3. Förster Resonance Energy Transfer (FRET)

3.3.1. FRET in Solid-State DSSCs Using TiO_2 Nanotubes. It is generally agreed that new materials as well as advanced device concepts are necessary for further improvements in efficiencies [66, 67]. The use of FRET has been contemplated as an alternative mechanism for charge separation and a way to improve exciton harvesting by placing the exciton close to the heterojunction interface [68]. In inorganic quantum-dot-based solar cells, the use of FRET to transfer the exciton generated in the quantum dot to a high mobility path, such as a nanowire or a quantum well, has been proposed as a way to bypass the traditional limitations of charge separation and transport [69].

In conventional DSSCs, a photoactive dye decorates the mesoporous TiO_2 film and the available empty space (porosities of ≈50% to 65% are common) [70] is filled with iodide-based redox electrolyte for dye regeneration. This reddish-brown nonphotoactive electrolyte also absorbs some portion of the visible light spectrum. To achieve a FRET-based photovoltaic architecture, we can effectively use this porous region by filling the pores of red/NIR light absorbing organic dye coated TiO_2 nanotubes with a mixture of spiro-OMeTAD and donor material—a high quantum yield, visible light absorbing fluorescent material. To improve device performance, the florescence spectrum of the donor molecules should match the optical absorption band of the absorber dye on the TiO_2. Further, the pore size dimensions should be small enough so that the nonradiative energy transfer events happen in close proximity. In the present work, the empty space (i.e., pores) of Red/Near IR absorbing SQ-1 organic dye [7, 71] coated transparent TiO_2 nanotube array films [35, 38, 72, 73], 500 to 600 nm in length with 20–28 nm pores on fluorine-doped tin oxide-coated glass, were filled with Spiro-OMeTAD [74] blended with a visible light absorbing 4-(dicyanomethylene)-2-methyl-6-(p-dimethylaminostyryl)-4H-pyran, DCM-pyran [75], donor molecules. The calculated Förster radius is 6.1 nm. The donor molecules contributed a FRET-based maximum IPCE of 25% with an increase in overall photoconversion efficiency by 76% [12].

Solid-state dye-sensitized solar cells (SS-DSSCs) have demonstrated open circuit photovoltages higher than their liquid-junction counterparts [15] and offer the prospect of an easily fabricated photovoltaic technology with relatively low material costs. In particular, SS-DSSC photovoltages of high value have been reported with the combined use of an organic sensitizer dye and hole transporting Spiro-OMeTAD [76–79]. This is attributed to the lower HOMO level of Spiro-OMeTAD in comparison to the redox potential of the I^-/I_2 electrolyte used in TiO_2-based liquid-junction DSSCs [15]. To increase SS-DSSC photoconversion efficiencies, numerous studies have investigated the use of high absorption coefficient dyes to increase light harvesting [79–82]. Higher device photoconversion efficiencies cannot be achieved simply by increasing device thickness; for example, Spiro-OMeTAD remains an effective hole transporting material for nanoporous dye-sensitized TiO_2 layers up to approximately 2.0 μm thick-for greater thicknesses issues of surface wetting and infiltration limits its successful application [83]. While organic dyes are known to strongly absorb light, enabling the use of thin layer devices, they do so only over a narrow spectral absorption bandwidth. Dye cocktails can potentially broaden the range of absorption; however, the coverage of one dye is generally at the expense of the other leading to relatively lower saturation photocurrents in their respective spectral absorption ranges [84–86].

There have been a few initial reports on the use of FRET [58] to enhance the efficiency of hybrid photovoltaic devices through increased light utilization [9–11, 13, 62, 87, 88]. In the FRET-based solid-state organic dye-sensitized solar cell possessing an extended photocurrent spectrum, the donor molecules embedded within the solid-state hole transporting material, Spiro-OMeTAD, absorb the high energy photons subsequently transferring the energy to the acceptor dye. Spiro-OMeTAD is a small organic molecule of high hole mobility, 10^{-4} cm^2/V·s, that is, noncrystalline in nature with a high glass transition temperature [89], properties that facilitate regeneration of the photo-excited acceptor dye. Spiro-OMeTAD is host for the donor molecules, and the Spiro-OMeTAD-donor dye mixture is intercalated within the acceptor dye-sensitized nanotube array films. The vertically oriented TiO_2 nanotube array morphology enables direct transport of the electrons injected from the photo-excited organic dye to the underlying FTO layer [27, 28]. The nanometer-scale nanotube pores, intercalated with the hole transporting materials, provide a facile path for hole transport. The energy level positions of the selected donor, DCM-pyran [75], and acceptor, SQ-1 dye [7], with respect to Spiro-OMeTAD [15, 90, 91] (Typical physical data of Spiro-OMeTAD, provided by EMD Chemicals (Merck KGaA, Darmstadt, Germany): HOMO energy ~ −4.9 eV, LUMO energy ~ −1.9 eV, Band gap ~3.0 eV, Glass transition temperature T_g ~120°C, Melting point T_m ~246°C, Purity >99.9% (Test procedure—HPLC). Note: the energy levels are determined using cyclic voltammetry and UV-VIS; these values are usually 0.2-0.3 eV less deep than with other optical methods (e.g., UPS).) and TiO_2 are shown in Figure 14. The selected donor, DCM-pyran, is a red arylidene laser dye with emission in the 570–620 nm range that is soluble in chlorobenzene (CB).

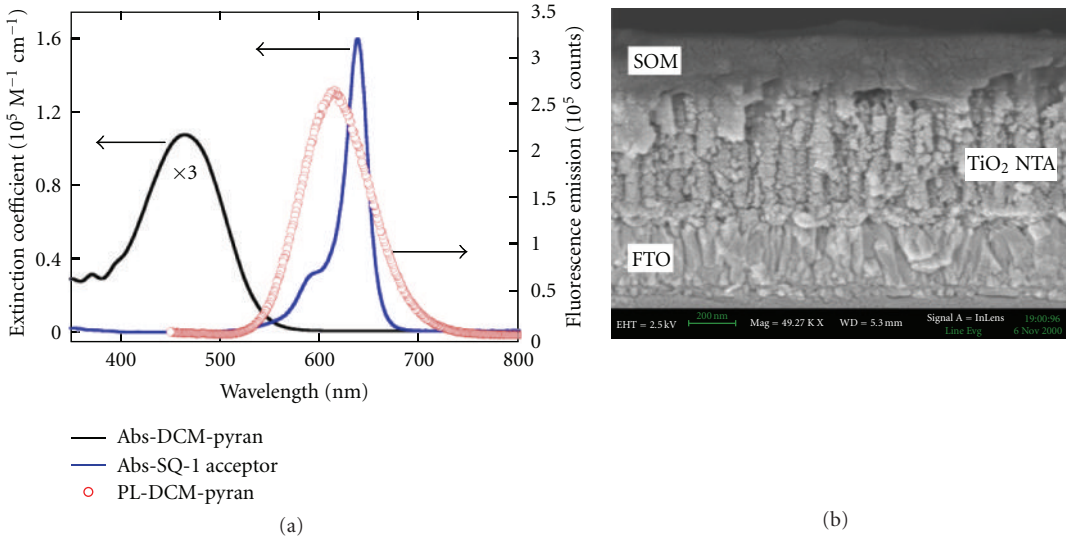

Figure 15: (a) Extinction coefficient of DCM-pyran donor and SQ-1 acceptor molecules dissolved in ethanol/acetonitrile-solvent mixture and the emission spectra of the same DCM-pyran solution. The DCM-pyran extinction coefficient is multiplied by 3 for display purposes. (b) Cross-sectional FE-SEM image showing DCM-Spiro-OMeTAD (denoted SOM) infiltration within SQ-1 dye-sensitized TiO_2 nanotube array (NTA, nanotube pore size ~20 to 28 nm, length ≈500 to 600 nm). FTO denotes the fluorine-doped tin oxide layer upon the glass substrate. Reprinted with permission from [12].

Figure 15(a) shows that a 7.2 μm DCM-pyran solution (DCM-pyran added in equal portions to a 1 : 1 ethanol:acetonitrile mixture) absorbs in the 350–550 nm wavelength range with a molar extinction coefficient of 37,900 $M^{-1}cm^{-1}$ at 460 nm; a fluorescence emission maximum is observed at 580 nm for a 430 nm excitation wavelength. The UV-VIS absorption spectrum of a 3.5 μm SQ-1 acceptor dye solution, in ethanol/acetonitrile, Figure 15(a), shows a molar extinction coefficient of 159,800 $M^{-1}cm^{-1}$ at a λ_{max} of 637 nm corresponding to strong π-π^* charge transfer transitions. As required for FRET, the fluorescence emission spectrum of DCM-pyran overlaps with the SQ-1 absorption spectrum. In calculating the spectral overlap integral from the normalized DCM-pyran photoluminescence and SQ-1 absorption spectra (in ethanol/acetonitrile), given a luminescence quantum yield (photons emitted to the number of photons absorbed by the sample) of 60% for DCM-pyran [92], assuming random orientation of the donor and acceptor molecules and an effective refractive index of Spiro-OMeTAD infiltrated TiO_2 nanotube arrays of 1.5, values ranging from 1.4 to 1.5 have been reported for liquid and Spiro-OMeTAD-based DSSC electrolytes [9–11], we calculate a Förster radius of 6.1 nm.

The SQ-1 dye absorption peak (in ethanol) broadens with sensitization of the TiO_2 nanotube array surface, with λ_{max} red shifted by 9 nm, and an FWHM of 100 nm versus 27 nm in the ethanol/acetonitrile mixture. The fluorescence spectrum of DCM-pyran mixed within Spiro-OMeTAD, with $Li(CF_3SO_2)_2N$ added to the Spiro-OMeTAD to enhance its hole mobility [93–95] then spin-coated onto TiO_2 nanotube films is also broadened, with the emission peak slightly blue shifted. This qualitative information indicates the potential for further enhancement of the spectral overlap integral value and hence a larger Förster radius. Figure 15(b) is an FE-SEM cross-sectional view of a DCM-Spiro-OMeTAD infiltrated SQ-1 dye-sensitized TiO_2 nanotube array film. The presence of FRET in our system was verified by observing the quenching of the fluorescence spectra of DCM-pyran donor molecules, dissolved in ethanol/acetonitrile, with a successive increase of SQ-1 dye concentration.

Starting with device Conc. SOM (30 μL SOM), which contains no DCM, see Table 2 and Figure 16(a), the IPCE is about 10% in the Red/NIR range; diluting the base solution with 15 μL CB, device Dilute SOM (+15 μL CB) shows a doubling of the Red/NIR IPCE to 20%. DCM-containing devices, DCM 10 to DCM 50 and DCM 30–48 mM, exhibit an IPCE of about 30–34% over the peak absorption wavelength corresponding to the SQ-1 dye, with the increase in donor concentration in turn diluting the Spiro-OMeTAD solution. As the 24 mM DCM-pyran solution volume increases from 10 μL to 50 μL, the visible region IPCE increases from 5 to 20%, further increasing to 25% for 30 μL of 48 mM DCM-pyran. The significant broad spectrum IPCE for such a thin-layer device indicates the great utility of FRET in enhancing solar cell efficiency. In comparison, recently phenanthroline ruthenium (II) was used as a phosphorescent energy relay dye in combination with unsymmetrical squaraine-sensitized nanoporous TiO_2 films 2.0 μm thick; the FRET-based contribution to the photocurrent generation in the visible range generated a maximum IPCE of about 8% [11]. With our 500–600 nm long nanotube-based films, we achieve continuous photocurrent generation over a broad spectral range, with the FRET-DCM donor contributed IPCE reaching 25% in the visible range and the acceptor contributed IPCE reaching 30–34% in the Red/NIR.

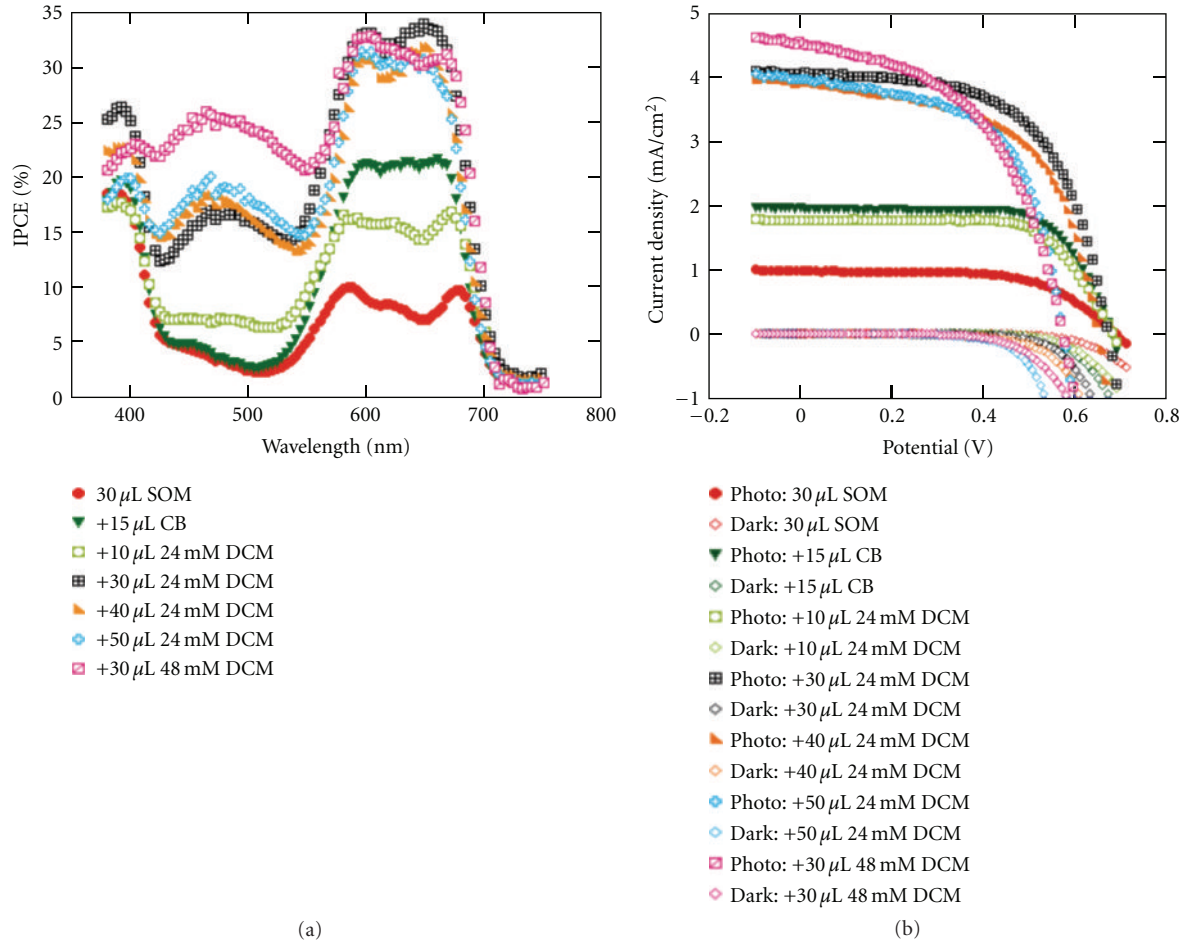

Figure 16: (a) IPCE of FRET-based SS-DSSC devices showing the effect of DCM amount and concentration added to 30 μL Spiro-OMeTAD-blend solution. All solutions were prepared in chlorobenzene. (b) Photocurrent density-Voltage, of FRET-based photovoltaic devices showing the effect of DCM amount and concentration added to 30 μL Spiro-OMeTAD-blend solution. All solutions were prepared in chlorobenzene (CB); the effect of diluting the Spiro-OMeTAD-blend with 15 μL CB is also illustrated. The DCM concentration is 24 mM except where noted. Optimal device performance was achieved with 30 μL of 24 mM DCM-pyran in 30 μL of 0.17 M Spiro-OMeTAD/0.12 M 4-tert butylpyridine/19.5 mM $Li[CF_3SO_2]_2N$, with the resulting (typical) device having a fill factor of 0.67, photovoltage of 0.68 V, J_{sc} of 4.05 mW/cm^2, and power conversion efficiency of 1.64%. Reprinted with permission from [12].

It was suspected that donor molecules near the center of the nanotube are too far from the SQ-1 dye layer, ≈10 to 14 nm, for FRET to occur hence energy is dissipated though fluorescence. However, use of smaller pore nanotubes poses the increased challenge of their uniform filling with the Spiro-OMeTAD solution. This can indirectly be judged by the effect of poor intercalation from the observation of below expected photocurrent generation in device Conc. SOM (30 μL SOM). For device Dilute SOM (+15 μL CB), the improved photocurrent is presumably due to efficient separation of the electron hole pairs photogenerated at the SQ-1 dye layer through the TiO_2 nanotubes and Spiro-OMeTAD, a behavior directly related to improved infiltration of Spiro-OMeTAD inside the nanotube arrays. In contrast, for the same device fabrication procedures, use of an excessively dilute base solution results in an extremely thin overlayer on top of nanotubes, reducing the shunt resistance between the dye-coated TiO_2 and gold electrode. Therefore, the performance of the FRET-based devices should be seen with respect to that of device Dilute SOM.

Figure 16(b) shows the photocurrent density-voltage characteristics of the SS-DSSC devices under 90 mW/cm^2 AM 1.5 G. Device photocurrent density exhibits a rapid increase in addition of up to 30 μL of 24 mM DCM-pyran solution, beyond which the photocurrent is reduced. Device photovoltage remains nearly constant to 40 μL of DCM-pryan solution, thereafter rapidly dropping. A maximum device efficiency η of 1.64% is achieved with a donor concentration of 30 μL of 24 mM DCM-pyran solution, device DCM 30, in 30 μL of 0.17 M Spiro-OMeTAD solution. The increase in device performance is attributed to the increased from 400 to 550 nm IPCE, see Figure 16(a). There is an optimum device composition for maximizing visible region photocurrent over which the photovoltage is not negatively affected. With increasing donor concentration in the base solution, see Table 2, the lithium salt and tert-butylpyridine

Table 2: Device names and their key fabrication details [12].

Device name	Volume of SOM—0.17 M/ Li salt—19.5 mM/ TBP—0.12 M in CB (μL)	Volume of DCM-pyran in CB Concentration—24 mM (μL)	Volume of DCM-pyran in CB Concentration—48 mM (μL)	Volume of CB (μL)	Wetting time before spin coating Sec.
Conc. SOM	30	—	—		60
Dilute SOM	30	—	—	15	90
DCM 10	30	10	—		75
DCM 30	30	30	—		90
DCM 40	30	40	—		120
DCM 50	30	50	—		120
DCM 30–48 mM	30	—	30		90

Note: SOM stands for Spiro-OMeTAD. Li salt for Bis(trifluoromethylsulfonyl)amine lithium salt, 99.95% trace metals basis. TBP for 4-*tert*-Butylpyridine. CB for Chlorobenzene. DCM-pyran for 4-(Dicyanomethylene)-2-methyl-6-(4-dimethylaminostyryl)-4*H*-pyran. Solutions were spin coated on SQ-1 acceptor dye-sensitized TiO_2 nanotubes at 2000 rpm. The 0.02 M $TiCl_4$-treated TiO_2 nanotubes are from 500 to 600 nm in length, and 20 to 28 nm pore size.

concentrations in the Spiro-OMeTAD decrease. It is known that the addition of lithium salt to Spiro-OMeTAD retards the recombination between electrons in the TiO_2 with holes in the Spiro-OMeTAD and increases the Spiro-OMeTAD conductivity [96, 97]. Hence a reduction of the lithium salt concentration in the Spiro-OMeTAD enhances the chances of electron-hole recombination, which in turn lowers the device photovoltage. Personal experience shows that Spiro-OMeTAD cells require a rather precise quantity and quality of lithium salt dopant for efficient performance. Without sufficient tert-butylpyridine to fill vacant sites on the TiO_2 surface, we may expect greater back-injection of electrons into the spiro-OMeTAD manifesting itself as a lower shunt resistance causing a drop in V_{oc}. This behavior is further supported by the performance of device DCM 30–48 mM, where the DCM concentration is doubled in the 30 μL CB solution; although the photocurrent of the resulting device is high, the photovoltage is low with the resulting $\eta = 1.32\%$.

To explore the possibility that diluting the spiro-OMeTAD additives caused our observed drop in V_{oc}, a cell was fabricated using a greater concentration of additives. For comparison, device Dilute SOM had an open circuit voltage of 0.69 V while device DCM 50 had an open circuit potential of 0.58 V. DCM 50 began with a solution of 0.17 M Spiro-OMeTAD in 30 μL chlorobenzene with 0.12 M tert-butylpyridine and 19.5 mM $Li[CF_3SO_2]_2N$ to which 50 μL of 24 mM DCM solution was added. The new test cell began with a solution of 0.17 M Spiro-OMeTAD in 30 μL chlorobenzene with 0.168 M tert-butylpyridine and 27.3 mM $Li[CF_3SO_2]_2N$, to which 50 μL of 24 mM DCM solution was added. By increasing the amount of additives to combat dilution by addition of DCM, the open circuit potential was raised from 0.58 V in DCM 50 to 0.67 V in the new test cell, favorably comparing to the V_{oc} value of 0.69 V in device Dilute SOM.

To help confirm the presence of FRET in our photovoltaic devices, we characterized the performance of device DCM 30, see Table 2, without a SQ-1 dye layer. The IPCE of the resulting device, Figure 17(a), due to electronic transfer of charge from the DCM molecules to the TiO_2 nanotube array surface, is approximately 3.15% in 400–600 nm wavelength range with essentially no photocurrent generation in the Red/NIR. This behavior indicates that the Red/NIR increase in IPCE with use of the DCM-diluted SOM solution is not due to the donor molecules themselves, but to improved infiltration of the DCM-SOM solution into the TiO_2 nanotubes, which increases the SQ-1 to spiro-OMeTAD contact area that in turn enables enhanced extraction of photocurrent from the SQ-1 molecules. The photovoltaic behavior of device DCM 30 fabricated without a SQ-1 dye layer on the TiO_2 surface is shown in Figure 17(b). The absence of the acceptor layer reduces the saturated photocurrent from 4.0 to 0.25 mA/cm^2 with the overall conversion efficiency dropping to $\eta = 0.13\%$. It is experimentally difficult to completely eliminate the possibility of some electronic transition from the DCM to SQ-1 molecules. However, this behavior is suggested by the low photocurrent generation from the TiO_2-DCM device, and the relatively close LUMO positions of the DCM and SQ-1 materials.

To determine the fraction of excited DCM donor molecules that transfer their energy to the SQ-1 acceptor dye-sensitized TiO_2 nanotube arrays, we calculate the excitation transfer energy (ETE) by the following relation [10, 11]:

$$\text{ETE} = \frac{\Delta\text{IPCE}}{\text{IQE} \cdot \eta_{\text{abs, donor}}}. \quad (1)$$

ΔIPCE represents the donor contributed IPCE, IQE is the device internal quantum efficiency, and $\eta_{\text{abs,donor}}$ the fraction of light absorbed by donor. For device DCM 30, the ΔIPCE (at 480 nm) is about 13.57%, $\eta_{\text{abs,donor}}$ (assuming 100% light absorption at 480 nm) is $\approx$62.5%, and IQE $\sim$ 41.6%, for an ETE of 52.2%. For device DCM 30–48 mM, ΔIPCE (at 480 nm) is about 22%, $\eta_{\text{abs,donor}}$ (at 480 nm) is $\approx$80.5%, and IQE $\approx$40.5% for an ETE of about 67.5%.

In FRET-type dye-sensitized solar cells, where Red/IR absorbing acceptor dyes are used to sensitize the TiO_2 and visible light absorbing donor molecules are mixed into the hole transporting spiro-OMeTAD or I^-/I_2, an excitation transfer efficiency (ETE) of up to 90% is needed

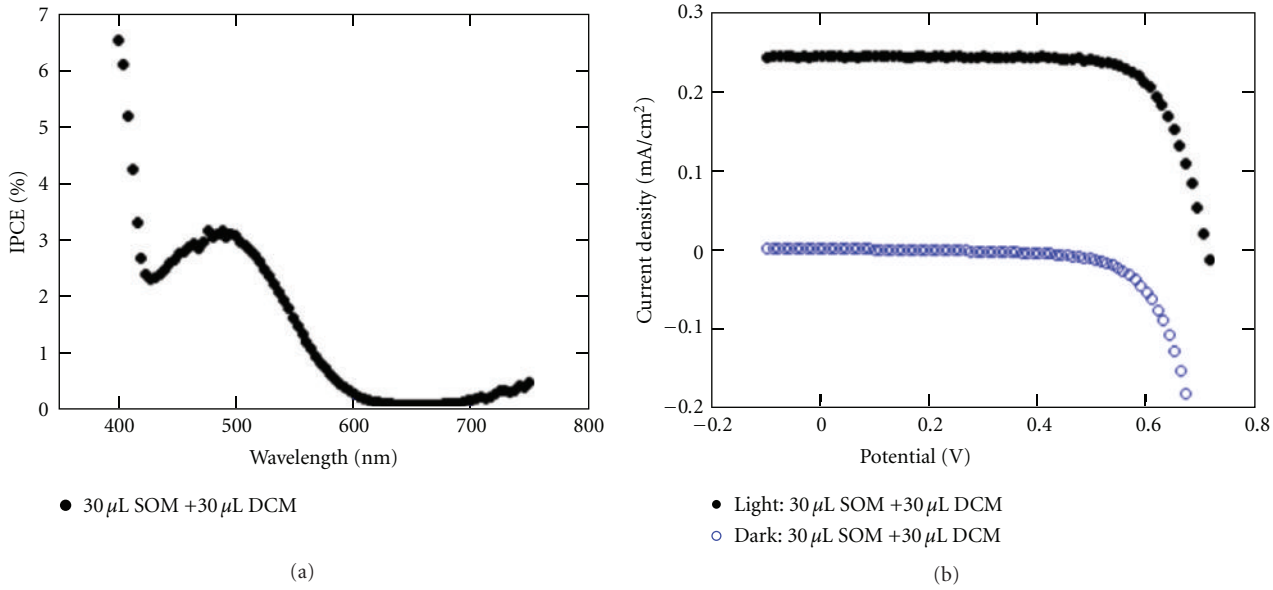

FIGURE 17: (a) The IPCE and (b) Photovoltaic behavior of a DCM 30-nanotube array device without a SQ-1 dye layer. J_{sc} is 0.25 mA/cm^2, V_{oc} = 0.71 V, FF = 0.74, and η = 0.13%. Reprinted with permission from [12].

to achieve record power conversion efficiencies. Recently, Hoke and coworkers analytically determined the ETE from donor to acceptor dyes within cylindrical and spherical pore geometries, correlating the ETE to the critical energy transfer distance (R_c) and the pore diameter [98]. They determined R_c by the following relation:

$$R_c = \left[\frac{C_A R_0^6}{1 + \tau_0 \sum_j k_{qj} \left[Q_j \right]} \right]^{1/4}. \quad (2)$$

R_o is the Förster radius, C_A is surface coverage concentration, τ_0 is the donor lifetime in the absence of a quencher, Q_j is the concentration of quenching species j, and k_{qj} is the bimolecular quenching coefficient for the donor-quencher combination.

For stationary donor and acceptor dyes within a cylindrical pore, achieving a 90% ETE requires an R_c equal to or greater than 0.3 of the pore diameter [98]. For an average 24 nm TiO_2 nanotube pore size, this implies that R_c should be greater than 7.2 nm. Assuming an SQ-1 dye surface concentration of 0.6 dye/nm^2, values from 0.2 to 1 dye/nm^2 have been reported [99], the calculated Förster radius of 6.1 nm, a DCM fluorescence lifetime of 1.6 ns [100], and approximating the $k_{qj}[Q_j]$ value as 10^9 M^{-1}s^{-1} [101], R_c is calculated to be 5.11 nm. Referring to Figure 2(c) of [98], such properties should result in an ETE value of approximately 70%, a value in excellent agreement with our 67.5% calculated ETE value.

3.3.2. FRET in Liquid-Junction DSSCs Using TiO_2 Nanowires. Shankar et al. demonstrated that an enhancement in photovoltaic device performance is possible using long-range resonance energy transfer from a dissolved luminescent dopant confined in the interstices of a nanowire array electrode to an acceptor species confined to the surface of the nanowires [9]. Shankar reported the use of FRET to boost the quantum yield for red photons at 675 to 680 nm by a factor of 4 for N-719 and a factor of 1.5 for black dye [9]. Figure 18 shows the optical properties of the dyes used. Phthalocyanines (traditionally acceptors) as energy donors and nonfluorescing ruthenium polypyridine complexes as acceptors were used. The bis(bipyridine) and terpyridine ruthenium complexes already have broad absorption in the visible region of the spectrum and excellent charge transfer characteristics, thus establishing a high baseline of light harvesting. The choice of phthalocyanines was driven by three considerations: light absorption, solubility, and aggregation. Zinc 2,9,16,23-tetra-*tert*-butyl-29*H*,31*H*-phthalocyanine (ZnPc-TTB) was chosen because the four tertiary butyl groups attached to the ZnPc core disrupt the formation of π-π stacking structures thereby reducing aggregation. Figure 18 presents the absorption and emission spectra of ZnPc-TTB, along with the absorption spectra of ruthenium polypyridine complex dyes. There is a significant overlap between the emission spectrum of ZnPc-TTB and the absorption spectrum of N-719, while for the donor and acceptor pair of ZnPc-TTB and black dye, the emission spectrum of the donor is completely contained within the absorption spectrum of the acceptor. The emission of ZnPc-TTB was found to quench by dilute solutions of N-719 and black dye, a necessary condition for FRET [9].

A key requirement for FRET is that the physical separation of the donor and acceptor species be close to the Förster radius for the donor-acceptor system. For this, 6 to 8 μm long extremely close-packed rutile TiO_2 nanowire array substrates, with an interwire spacing of 5 to 10 nm, were used. The acceptor dye molecule is anchored to the surface of the nanowires. Due to the confinement of

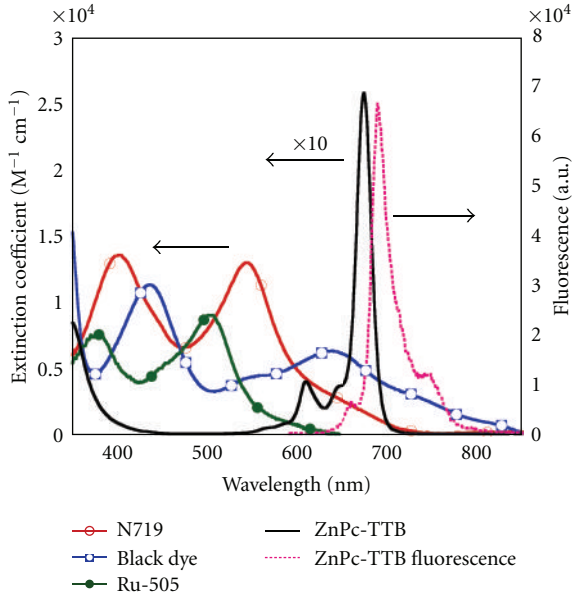

Figure 18: Absorption spectra of donor and acceptor dyes and emission spectrum of phthalocyanine donor. For display purposes, 0.1 times the extinction coefficient of ZnPc-TTB is shown. Reprinted with permission from [9].

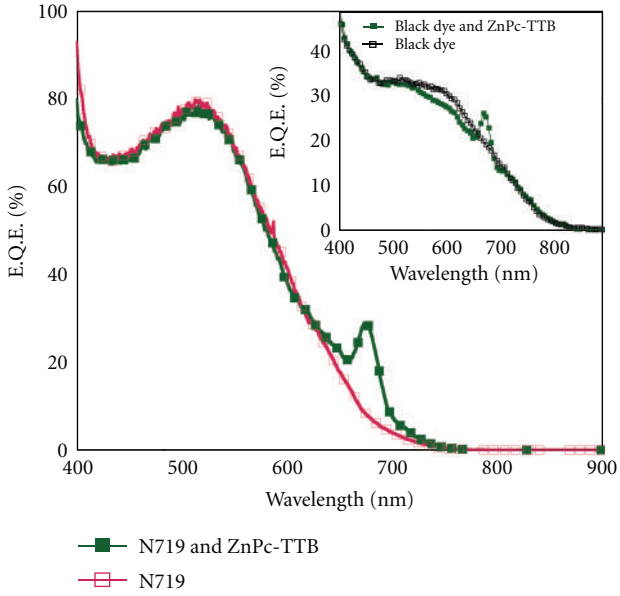

Figure 19: Action spectrum of nanowire solar cell comprising N-719-coated rutile as acceptors, with and without ZnPC-TTB molecules in electrolyte as the donors. Inset shows action spectrum for black-dye-coated rutile acceptors with and without ZnPc-TTB donors. Ten percent of data points are shown. Reprinted with permission from [9].

the liquid electrolyte in the nanowire array interstices, a large number of donor dye molecules dissolved in solution are effectively within a Förster radius of the acceptor molecules, thus facilitating energy transfer between donor and acceptor molecules. However, energy transfer in this device architecture of solution-based donors and surface-confined acceptors can be better represented by a system consisting of energy transfer from a donor chromophore to a two-dimensional sheet of acceptors at a distance d. For this geometry, Kuhn showed that the rate of energy transfer follows the inverse fourth power of the interchromophoric distance [103].

In this device configuration, ZnPc-TTB molecules were introduced directly into the tri-iodide redox electrolyte at a (high) concentration of 1–5 mg/mL. As seen in Figure 19, a dramatic increase in the quantum yield for red photons in the spectral region of 670–690 nm was immediately observed, over and above the quantum yields exhibited by N-719 and black-dye-sensitized nanowire solar cells. N-719 dye forms a nonagglomerated monolayer [104]. Since black dye agglomerates, coadsorption of deoxycholic acid was employed to form the black dye coating and reduce agglomeration [105]. The dilution of black dye in the monolayer reduced the concentration of acceptors available for energy transfer and resulted in lower critical distance and lower energy transfer efficiencies for black dye relative to N-719 despite the higher spectral overlap of black dye absorption with the emission spectrum of ZnPc. Resonance energy transfer of excitons generated in ZnPc-TTB molecules from red photons to surface bound N-719 dye results in a fourfold enhancement of quantum yield at 675 to 680 nm. Since the extinction coefficient of ZnPc-TTB molecules in the spectral region of 670−690 nm is far greater than that of N-719, we believe the entire quantum yield of 28% at the donor absorption maximum is attributable to FRET and is close to the measured fluorescence quantum yield of ZnPc-TTB in solution [106]. At the high concentrations used, zinc phthalocyanine forms multimolecular aggregates with a reduced quantum yield due to concentration quenching. A self-sieving effect of the nanowires admitting only monomeric and dimeric forms into the interwire spaces may account for the nearly quantitative efficiency of energy transfer from ZnPC-TTB in solution to surface-anchored N-719 and black dye molecules, a hypothesis supported by the saturation of the external quantum yields for red photons at values close to the fluorescence quantum yield of the donor.

3.4. Liquid-Junction DSSCs. The building blocks of these solar cells are a photoanode consisting of high surface area TiO_2 anatase nanoparticle film (thickness ~10 μm) on transparent conducting oxide (TCO) glass, upon which the illumination is incident, supporting a monolayer of a light absorbing chromophore, an iodide electrolyte, and a platinum-coated TCO glass counter electrode. High efficiency DSSCs are commonly achieved with the help of a 4 μm thick layer of TiO_2 particles, approximately 400–800 nm in diameter, atop the transparent photoanode to scatter red and near-infrared wavelengths so as to enhance absorption by the dye molecules [107, 108].

The excitons generated in the dye (normally a ruthenium polypyridyl complex) as a result of light absorption are instantaneously split, with electrons injected into the nanoparticle film and holes released to oxidize iodide

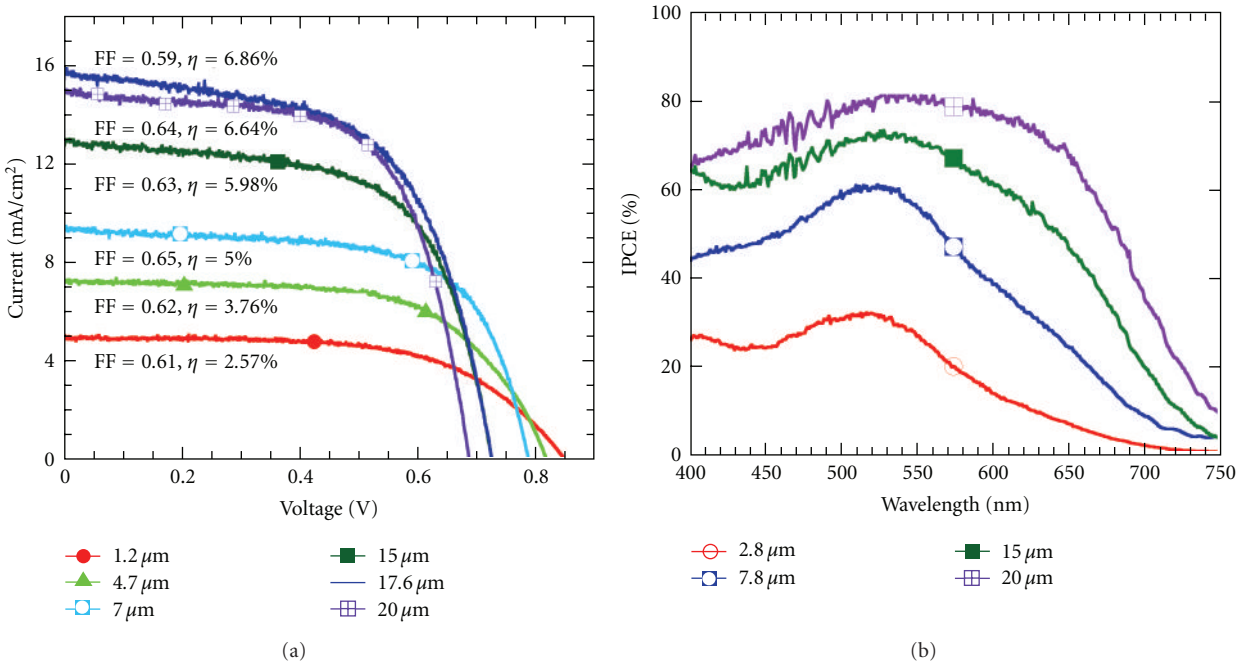

FIGURE 20: (a) Current-voltage characteristics of DSSCs fabricated using transparent nanotube array films of various lengths. The pore size of the 1.2 μm film was 58 nm, while it was 95 nm for the rest of the films. The 20 μm long nanotubes were fabricated from a 12 μm thick Ti film. (b) The IPCE spectra of DSSCs fabricated using transparent nanotube array films of various lengths. Reprinted with permission from [35].

species in the electrolyte. The electrons diffuse through the nanoparticle network and are collected at the TCO. The electrons, while percolating through the randomly oriented nanoparticle network, undergo many trapping and detrapping events at defect states before combining with oxidized electrolyte species or reaching the TCO layer. The electron diffusion length of these films, as determined using intensity-modulated photovoltage and photocurrent spectroscopies (IMVS and IMPS, resp.), is in the range of 10–30 μm [109]. Hence an increase in the nanoparticle film thicknesses significantly above 10 μm, in order to absorb low energy photons (red and near-infrared wavelengths) that are weakly absorbed by commonly used ruthenium bi or terpyridyl complexes, does not generally result in an increase of the photoconversion efficiency. The potential for future increases in DSSC efficiency relies largely on the invention of new dyes, ideally those offering large extinction coefficients and broad spectrum absorption, and on the development of highly ordered material architectures offering longer electron diffusion lengths and shorter electron transport time constants than those in conventional randomly oriented nanoparticle films. With this as motivation, other wide bandgap oxide semiconductors and different architectures have been investigated as alternatives to the nanoparticle films [24, 110, 111].

3.4.1. Short and Long TiO_2 Nanotubes. A promising nanoarchitecture for solar energy conversion within a DSSC is an array of highly ordered, vertically aligned TiO_2 nanotubes grown by anodic oxidation of titanium [54, 112] offering electron transport properties superior to films comprised of randomly oriented TiO_2 nanoparticles. Zhu et al. have shown that (back side illuminated) dye-sensitized solar cells, fabricated using TiO_2 nanotube arrays grown on titanium foil, have a charge collection efficiency 25% higher, and a light harvesting efficiency 20% higher, than corresponding nanoparticle-based DSSCs [28]. The higher light harvesting efficiency has been attributed to the enhanced light scattering properties of the TiO_2 nanotube arrays. In a more recent work, Jennings and coworkers estimated the electron diffusion length in TiO_2 nanotube arrays on titanium foil by considering the electron diffusion coefficient and life time as a function of electron quasi-Fermi level and obtained a value of 100 μm, which is at least 3× better than that in the case of nanoparticle film-based DSSCs [29]. Thus TiO_2 nanotube-array-based DSSCs offer the prospect of photoelectrodes having much greater thicknesses without a corresponding decrease in performance due to unwanted charge recombination. Thicker photoelectrodes would enable the harvesting of low energy photons using either a single dye, or different dyes covering different regions of the nanotube length, with a dye sensitive to shorter wavelengths at the illuminated end of the film, and a dye sensitive to longer wavelengths at the other.

The current-voltage characteristics of dye-sensitized solar cells fabricated using TiO_2 nanotubes of length up to 20 μm are shown in Figure 20(a). The DSSC employing 17.6 μm long nanotubes, fabricated from 20 μm thick Ti films yielded a power conversion efficiency of 6.9% (V_{oc} = 0.73 V, J_{sc} = 15.8 mA/cm^2 and FF = 0.59). In comparison, in high efficiency nanoparticle DSSCs (power efficiency 10-11%)

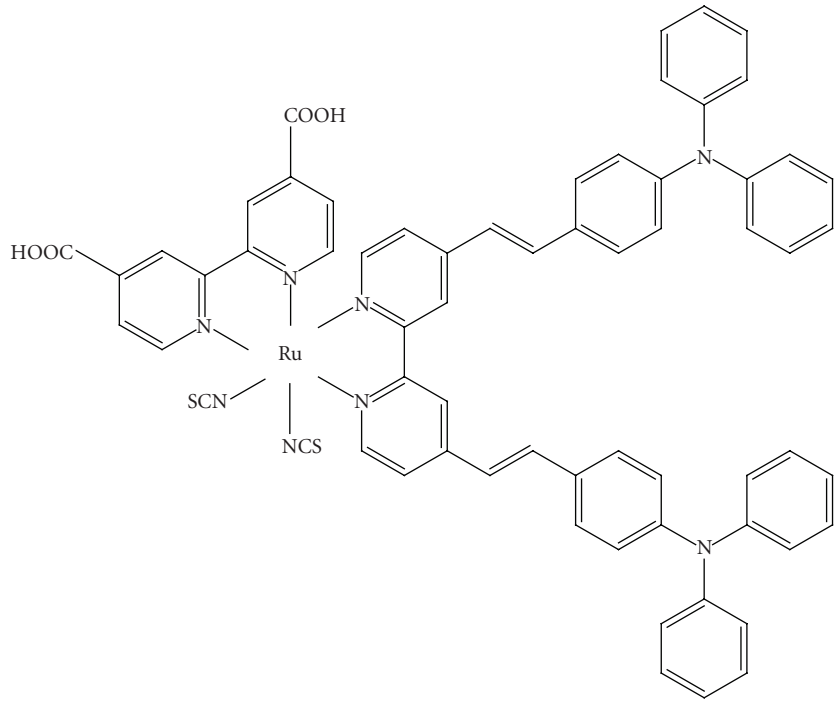

Figure 21: Molecular structure of Ru-TPA-NCS. Reprinted with permission from [102].

fabricated under highly optimized conditions (e.g., using highly purified dyes, nanoparticle scattering layer, etc.), the J_{sc} is about 17-18 mA/cm^2, the fill factor is close to 0.75, and V_{oc} is 0.7–0.85 V [107, 108]. Considering that we used commercially available N719 dye without further purification and that the roughness factor was slightly lower, about 900 for 20 μm long nanotubes versus over 1000 for nanoparticle films of thickness 10–12 μm, the J_{sc} value obtained is remarkable. The major factor that limits the power efficiency of nanotube-array DSSCs is their low fill factor, about 25% lower than their nanoparticle counterparts. This is largely due to an increase in the width of the TiO_2 nanotube array-FTO interfacial layer, which occurs during annealing of the nanotube array samples as required for crystallization and to oxidize trace metal particles within the nanotube film. Higher efficiencies should be possible with elimination of this problem and using nanotubes of greater roughness factor-that is, smaller pore diameter and/or greater lengths.

Figure 20(b) shows the IPCE spectra obtained from nanotube array DSSCs. The IPCE is as high as from 70 to 80% in a wide wavelength range (450 to 650 nm) and has a significant magnitude up to 700 nm. The projection of the shoulder in the wavelength region above 600 nm with increasing nanotube length shows efficient conversion of low energy photons without the need of a scattering layer as used in high efficiency nanoparticle DSSCs [107, 108]. The IPCE spectrum of the DSSC employing 20 μm long nanotubes closely follows the transmittance spectrum of the TEC 8 glass substrate. The loss due to light absorption at 500 nm by the electrolyte trapped in the pores is ~1% (estimated from electrolyte absorbance), which is lower at higher wavelengths. Thus the internal quantum efficiency of the device approaches 95–100% in this wavelength region; that is, about 95–100% of the absorbed photons having energy in this region are converted into electrons in the external circuit even though the thickness of the nanotube film is twice that of nanoparticle films used in high-efficiency DSSCs. This clearly shows that DSSCs can effectively employ nanotubes of still greater lengths; however, making such long tubes is a great challenge.

3.4.2. TiO_2 Nanotubes and Donor Antenna Dyes. The donor-antenna dye *cis*-di(thiocyanato)(2,2′-bipyridyl-4,4′-dicarboxylic acid)-(2,2′-bipyridyl-4,4′-bis(vinyltriphenyl amine) ruthenium(II) (named as Ru-TPANCS) contains the electron-rich donor triphenylamine linked to the bpy by a conjugated vinyl spacer. The molecular structures of the Ru-TPA-NCS donor-antenna dye and the commercially available N-719 dye (Solaronix) are shown in Figure 21, respectively. The extended π electron delocalization in the bpy ligand enables the donor-antenna dye molecules to have high molar extinction coefficients, more than twice that of the commonly used N-719 dye [113]. Furthermore, unlike in N-719, the HOMO of Ru-TPA-NCS are spread over the triphenyl amine moieties [114, 115]. The increased separation of the HOMO levels from the TiO_2 surface has been shown to retard the recombination process at the TiO_2-dye interface and at the TiO_2-hole conductor interface in solid-state solar cells [116]. The procedures for the synthesis of the donor-antenna dye are detailed elsewhere [116].

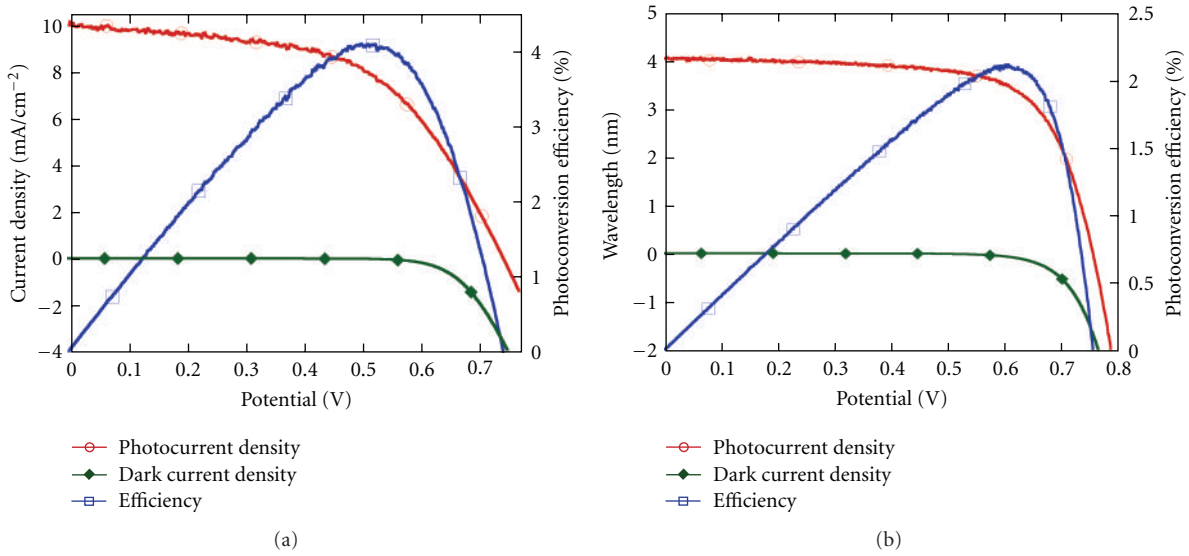

FIGURE 22: (a) Current-voltage characteristics of frontside illuminated solar cells with Ru-TPANCS-sensitized 1 μm long $TiCl_4$-treated TiO_2 nanotube array under 1 sun AM 1.5 illumination. (b) AM 1.5 current-voltage characteristics of a $TiCl_4$-treated 1 μm long transparent nanotube array with N-719. Reprinted with permission from [102].

The donor-antenna dye Ru-TPA-NCS exhibits 4-5 times higher molar extinction coefficient than N-719 at 400 nm [113]. Because of the much higher molar extinction coefficient of the Ru-TPA-NCS dye, a much lower film thickness should suffice to harvest a similar amount of incident photons. Shankar et al. employed vertically oriented TiO_2 nanotube arrays in conjunction with the Ru-TPA-NCS donor-antenna dye to fabricate liquid-junction dye-sensitized solar cells [102]. It was noted that the TiO_2 NT array electrode sensitized with Ru-TPA-NCS dye has higher optical absorption than the N-719-coated sample across the entire solar spectrum with an absorbance more than twice that of the N-719 dye at 470 nm, which corresponds to the wavelength of maximum irradiance in the solar spectrum. Front side illumination was employed using 1 μm long transparent nanotube arrays, with an average pore diameter of 100 nm, on FTO-coated glass [72]. The $TiCl_4$-treated transparent nanotube arrays were sensitized with Ru-TPA-NCS dye and used to fabricate solar cells, whose I-V characteristics are shown in Figure 22(a). With transparent nanotube arrays, the commercially available redox electrolyte MPN-100 (Solaronix) containing 100 mM of tri-iodide in methoxypropionitrile was used. Figure 22(a) shows that a 1 μm long TiO_2 nanotube array yields a short circuit photocurrent density of 10.1 mA/cm^2, an open circuit potential of 743 mV, and a fill factor of 0.55 resulting in an overall conversion efficiency of 4.1%. Figure 23(b) presents the performance of a similar solar cell constructed by sensitizing a $TiCl_4$-treated 1 μm long transparent nanotube array with N-719. While the use of N-719 results in slightly larger values of the open circuit potential, the short circuit photocurrent density J_{sc} is nearly half that obtained with Ru-TPA-NCS sensitization because of the smaller amount of light harvested.

3.4.3. TiO_2 Nanowire Arrays. Rutile TiO_2 nanowire array samples were sensitized with a monolayer of dye by immersion overnight in a 0.5 mM N719 solution. A liquid-junction solar cell was prepared by infiltrating the dye-coated TiO_2 electrode with commercially available redox electrolyte MPN-100 (Solaronix) containing 100 mM of tri-iodide in methoxypropionitrile. A conductive glass slide sputter-coated with 100 nm of Pt was used as the counter-electrode. Electrode spacing between the nanowire and counter-electrodes was assured by the use of a 25 μm thick SX1170 spacer. Photocurrent density and photovoltage of the prepared DSSCs were measured with active sample areas of 0.4-0.5 cm^2 under AM-1.5 G simulated sunlight.

Figure 23(a) shows the J-V characteristics of a typical 2-3 μm nanowire length sample grown directly on the FTO-coated substrate. An overall photoconversion efficiency of 4.35% was achieved (V_{oc} = 0.758 V, J_{sc} = 10.2 mA/cm^2, and FF = 0.56). Table 3 includes statistical data related to the performance of solar cells comprising nanowire arrays of different lengths. By using the same batch of N-719 dye, the same redox electrolyte, and similar active areas, we sought to isolate the effect of nanowire length on device performance. Normally, the surface area and hence the dye adsorbed increases as a function of length because of which an increase in solar cell performance with nanowire length is expected. However, here it was observed that wires 2-3 μm long exhibited the best performance with an average efficiency of 4.83%, with decreasing performance seen for longer nanowires. This can be understood within the context of nanowire array formation. Longer nanowire arrays result when the duration of the hydrothermal growth is extended; the longer times cause an increase in the lateral dimension as well as the axial dimension of the nanowires. An increase in nanowire width decreases the packing density per unit area of

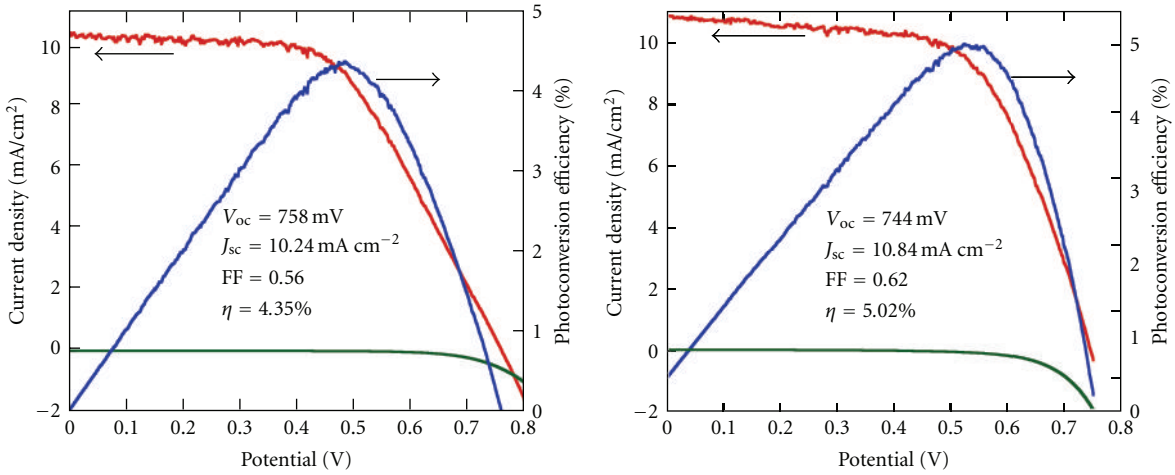

Figure 23: Photocurrent density, dark current density, and power density of 2.0 μm long rutile TiO_2 nanowire-array-based dye-sensitized solar cells under AM 1.5 illumination (100 mW/cm^2): (a) unmodified nanowire array grown directly on TCO substrate and (b) a $TiCl_4$ treatment is used to coat the TCO substrate prior to nanowire array growth and a $NbCl_5$ treatment used on the nanowires prior to device assembly. Reprinted with permission from [24].

Table 3: Statistics of TiO_2 nanowire arrays dye-sensitized solar cells showing the mean (μ), and standard deviation (σ) of the solar cell parameters: Short Circuit Photocurrent Density (J_{sc}), Open Circuit Voltage (V_{oc}), Fill Factor, and Efficiency (η) [102].

Length of nanowires (μm)	Typical nanowires width (nm)	No. of devices	μ_{Jsc}	σ_{Jsc}	μ_{Voc}	σ_{Voc}	μ_{ff}	σ_{ff}	μ_{η}	σ_{η}
2-3	10–15	6	10.3	2.52	751	36	0.57	0.05	4.34	1.09
3-4	20–25	6	8.47	1.06	742	21	0.6	0.05	3.75	0.39
4-5	30–35	10	7.29	2.29	769	19	0.62	0.04	3.39	0.85

the nanowire arrays, which results in lower effective internal surface area available for dye adsorption despite the higher length. It was also noted that the extended reaction times, corresponding to nanowire arrays longer than 4 μm, weaken the nanowire-FTO interface, with the resulting samples demonstrating poorer photoelectrochemical properties.

The device photoconversion efficiency could be improved in the following manner. To improve the fill factor, after the TiO_2 nanowire growth, an overlayer of niobium oxide was subsequently coated onto the nanowires, which was found to improve the efficiency by reducing recombination [117, 118]. To form the Nb_2O_5 coating, the prepared nanowire samples were dipped in a 5 mM $NbCl_5$ dry ethanol solution, then heated in air at 500°C for 0.5 h [118]. Figure 23(b) shows the J-V characteristics of a typical 2-3 μm long Nb_2O_5-treated nanowire array device under AM 1.5 illumination. An overall photoconversion efficiency, after much work, of 5.02% was achieved (V_{oc} = 0.744 V, J_{sc} = 10.84 mA/cm^2, and FF = 0.62).

We note that in spite of their superior charge transport characteristics, 20 μm long ZnO nanowire arrays exhibit relatively low efficiencies when used in dye-sensitized solar cells due to poor dye adsorption [110]. We attribute our much higher light-to-electricity conversion efficiency achieved using rutile TiO_2 nanowire arrays to the ability of the dye to anchor on the (110) crystal plane, which is both stable and has a strong interaction with carboxylate groups of the N719 dye molecule [119]. In contrast, the acidic carboxylate groups of the dye dissolve the outer layer of the ZnO surface forming a Zn^{2+}-dye complex layer [120, 121], which in turn weakens the interaction of the dye with the electrode surface. Solar cells comprising 2 μm long rutile nanowires exhibit higher efficiencies than rutile nanoparticulate films thicker than 5 μm [122]. Efficient vectorial charge transport, enabled by the single crystal nanowires, leads us to believe that significantly higher efficiencies can reasonably be expected through solution of the interface problem and nanowire-bunching presently seen in rutile TiO_2 nanowire arrays longer 4 μm, which would enable greater light absorption without a corresponding penalty in charge transfer capabilities. Of course, the ability to synthesize self-assembled, single-crystal, vertically oriented anatase nanowires directly onto a transparent conductive oxide-coated substrate, without damage to the substrate, would be a tremendous step-forward in the dye-sensitized solar cell field.

4. Conclusions

We have reviewed the fabrication of self-assembled vertically oriented 1D TiO_2 nanostructures such as nanotube/nanowire arrays and their application in various excitonic solar cells such as bulk heterojunction, ordered heterojunction, FRET-type solid-state and liquid-based DSSCs. Self-organized and vertically oriented TiO_2 nanotube arrays

were grown on FTO glass by anodic oxidation of thin/thick Ti films in fluoride ions containing DMSO or EG-based organic solvents. A small amount of water is added in the solution to obtain debris-free nanotube arrays. Small pore size nanotubes, necessary for high surface area films, are possible in shorter length tubes; the pore size increases if we need longer length tubes which require greater anodization voltages. It was shown that transparent TiO_2 nanotube arrays films on transparent conducting oxide glass could be fabricated with lengths between 0.3 and 33.0 μm. Short nanotube array films showed strong antireflection properties, while films of longer nanotube arrays suffered from imperfect light transmission properties due to residual metal atoms. In liquid-junction DSSCs comprised of 17.6 μm long TiO_2 nanotubes coated with N719 dye, a photoconversion efficiency of 6.9% was obtained, with an IPCE of 70 to 80% between 450 and 650 nm.

In bulk heterojunction solar cells, short length tubes (270 nm long and 50 nm pore size prepared by anodization in aqueous HF bath) were filled with a P3HT + PCBM mixture to achieve a photoconversion efficiency of about 4.1%. Given the hydrophilic nature of TiO_2, the hydrophobic nature of P3HT, and the relatively small pore size (~35 nm) of 700–800 nm long, nanotubes infiltration of this blend into the nanotube array pores was difficult. Various organic solvents were used to change the surface wetting properties before polymer filling. Further, these solvents were required to mix well with the polymer blend and then evaporate during the spin-coating process. With such solvents, we achieved greater percolation of the P3HT/PCBM blend inside the nanotube arrays; however, this process appears to change the configuration of the polymer chain leading to a reduction in the device photovoltage.

In fabrication of ordered heterojunction solar cells, an organic dye was anchored to the TiO_2 as an intermediate layer to promote electronic transitions, and to broaden the spectral absorption band with the SQ-1 dye absorbing Red/NIR light and P3HT absorbing in the visible. The HOMO-LUMO levels of the dye and polymer, and the conduction band level of TiO_2 are such that the electrons flow towards the TiO_2 while holes are transported to the opposite electrode. Without the use of fullerene derivatives, we achieved a photoconversion efficiency of approximately 4%.

In FRET-type solar cells, we filled the empty space, normally used for filling with redox electrolyte in liquid-junction DSSCs, in dye-sensitized TiO_2 nanotube arrays with a blend of spiro-OMETAD and DCM (visible light absorbing molecules). To achieve FRET, it is necessary for the DCM photoluminescence to significantly match with the spectral absorption of the anchoring SQ-1 dye. The DCM donor molecules contributed a FRET-based maximum IPCE of 25%. An excitation transfer efficiency of about 67.5% was achieved and a 76% increase in the photoconversion efficiency in our optimal devices. In liquid-based DSSCs, using Förster-type resonance energy transfer from zinc phthalocyanine donor molecules to ruthenium polypyridine complex acceptors results in a fourfold increase in quantum yields for red photons in dye-sensitized nanowire array solar cells. The spatial confinement of the electrolyte imposed by the wire-to-wire spacing of the close-packed nanowire array architecture ensures that the distances between a significant fraction of donors and acceptors are within a Förster radius.

Acknowledgment

The authors acknowledge support from the Natural Science Foundation of China under Award no. 21006044.

References

[1] O. K. Varghese and C. A. Grimes, "Appropriate strategies for determining the photoconversion efficiency of water photoelectrolysis cells: a review with examples using titania nanotube array photoanodes," *Solar Energy Materials and Solar Cells*, vol. 92, no. 4, pp. 374–384, 2008.

[2] Z. Li, K. Shankar, G. K. Mor et al., "Functionalized pentacenes for dye-sensitized solar cells," *Journal of Photonics for Energy*, vol. 1, Article ID 011106, 2011.

[3] S.-T. Fei, S.-H. A. Lee, S. M. Pursel et al., "Electrolyte infiltration in phosphazene-based dye-sensitized solar cells," *Journal of Power Sources*, vol. 196, no. 11, pp. 5223–5230, 2011.

[4] J. Bandara, K. Shankar, J. Basham et al., "Integration of TiO_2 nanotube arrays into solid-state dye-sensitized solar cells," *EPJ Applied Physics*, vol. 53, no. 2, Article ID 20601, 2011.

[5] Q. Kang, S. H. Liu, L. X. Yang, Q. Y. Cai, and C. A. Grimes, "Fabrication of PbS nanoparticle sensitized TiO_2 nanotube arrays and their photoelectrochemical properties," *ACS Applied Materials & Interfaces*, vol. 3, pp. 746–749, 2011.

[6] M. C. Scharber, D. Mühlbacher, M. Koppe et al., "Design rules for donors in bulk-heterojunction solar cells—towards 10 % energy-conversion efficiency," *Advanced Materials*, vol. 18, no. 6, pp. 789–794, 2006.

[7] G. K. Mor, S. Kim, M. Paulose et al., "Visible to near-infrared light harvesting in TiO_2 nanotube array-P3HT based heterojunction solar cells," *Nano Letters*, vol. 9, no. 12, pp. 4250–4257, 2009.

[8] M. D. McGehee, "Nanostructured organic-inorganic hybrid solar cells," *MRS Bulletin*, vol. 34, no. 2, pp. 95–100, 2009.

[9] K. Shankar, X. Feng, and C. A. Grimes, "Enhanced harvesting of red photons in nanowire solar cells: evidence of resonance energy transfer," *ACS Nano*, vol. 3, no. 4, pp. 788–794, 2009.

[10] B. E. Hardin, E. T. Hoke, P. B. Armstrong et al., "Increased light harvesting in dye-sensitized solar cells with energy relay dyes," *Nature Photonics*, vol. 3, no. 7, pp. 406–411, 2009.

[11] J. H. Yum, B. E. Hardin, S. J. Moon et al., "Panchromatic response in solid-state dye-sensitized solar cells containing phosphorescent energy relay dyes," *Angewandte Chemie - International Edition*, vol. 48, no. 49, pp. 9277–9280, 2009.

[12] G. K. Mor, J. Basham, M. Paulose et al., "High-efficiency förster resonance energy transfer in solid-state dye sensitized solar cells," *Nano Letters*, vol. 10, no. 7, pp. 2387–2394, 2010.

[13] J. I. Basham, G. K. Mor, and C. A. Grimes, "Förster resonance energy transfer in dye-sensitized solar cells," *ACS Nano*, vol. 4, no. 3, pp. 1253–1258, 2010.

[14] S. Buhbut, S. Itzhakov, E. Tauber et al., "Built-in quantum dot antennas in dye-sensitized solar cells," *ACS Nano*, vol. 4, no. 3, pp. 1293–1298, 2010.

[15] P. Chen, J. H. Yum, F. De Angelis et al., "High open-circuit voltage solid-state dye-sensitized solar cells with organic dye," *Nano Letters*, vol. 9, no. 6, pp. 2487–2492, 2009.

[16] G. K. R. Senadeera, P. V. V. Jayaweera, V. P. S. Perera, and K. Tennakone, "Solid-state dye-sensitized photocell based on pentacene as a hole collector," *Solar Energy Materials and Solar Cells*, vol. 73, no. 1, pp. 103–108, 2002.

[17] B. O'Regan and M. Grätzel, "A low-cost, high-efficiency solar cell based on dye-sensitized colloidal TiO_2 films," *Nature*, vol. 353, no. 6346, pp. 737–740, 1991.

[18] S. H. Park, A. Roy, S. Beaupré et al., "Bulk heterojunction solar cells with internal quantum efficiency approaching 100%," *Nature Photonics*, vol. 3, no. 5, pp. 297–303, 2009.

[19] H. Y. Chen, J. Hou, S. Zhang et al., "Polymer solar cells with enhanced open-circuit voltage and efficiency," *Nature Photonics*, vol. 3, no. 11, pp. 649–653, 2009.

[20] http://www.solarmer.com/, http://www.plextronics.com/index.aspx, http://www.konarka.com/.

[21] K. Nakayama, K. Tanabe, and H. A. Atwater, "Plasmonic nanoparticle enhanced light absorption in GaAs solar cells," *Applied Physics Letters*, vol. 93, no. 12, Article ID 121904, 2008.

[22] A. Luque, A. Martí, and A. J. Nozik, "Solar cells based on quantum dots: multiple exciton generation and intermediate bands," *MRS Bulletin*, vol. 32, no. 3, pp. 236–241, 2007.

[23] A. G. Pattantyus-Abraham, I. J. Kramer, A. R. Barkhouse et al., "Depleted-heterojunction colloidal quantum dot solar cells," *ACS Nano*, vol. 4, no. 6, pp. 3374–3380, 2010.

[24] X. Feng, K. Shankar, O. K. Varghese, M. Paulose, T. J. Latempa, and C. A. Grimes, "Vertically aligned single crystal TiO_2 nanowire arrays grown directly on transparent conducting oxide coated glass: synthesis details and applications," *Nano Letters*, vol. 8, no. 11, pp. 3781–3786, 2008.

[25] G. K. Mor, K. Shankar, M. Paulose, O. K. Varghese, and C. A. Grimes, "Use of highly-ordered TiO_2 nanotube arrays in dye-sensitized solar cells," *Nano Letters*, vol. 6, no. 2, pp. 215–218, 2006.

[26] D. Gong, C. A. Grimes, O. K. Varghese et al., "Titanium oxide nanotube arrays prepared by anodic oxidation," *Journal of Materials Research*, vol. 16, no. 12, pp. 3331–3334, 2001.

[27] M. Paulose, K. Shankar, S. Yoriya et al., "Anodic growth of highly ordered TiO_2 nanotube arrays to 134 μm in length," *Journal of Physical Chemistry B*, vol. 110, no. 33, pp. 16179–16184, 2006.

[28] K. Zhu, N. R. Neale, A. Miedaner, and A. J. Frank, "Enhanced charge-collection efficiencies and light scattering in dye-sensitized solar cells using oriented TiO_2 nanotubes arrays," *Nano Letters*, vol. 7, no. 1, pp. 69–74, 2007.

[29] J. R. Jennings, A. Ghicov, L. M. Peter, P. Schmuki, and A. B. Walker, "Dye-sensitized solar cells based on oriented TiO_2 nanotube arrays: transport, trapping, and transfer of electrons," *Journal of the American Chemical Society*, vol. 130, no. 40, pp. 13364–13372, 2008.

[30] H. E. Prakasam, K. Shankar, M. Paulose, O. K. Varghese, and C. A. Grimes, "A new benchmark for TiO_2 nanotube array growth by anodization," *Journal of Physical Chemistry C*, vol. 111, no. 20, pp. 7235–7241, 2007.

[31] S. Yoriya, G. K. Mor, S. Sharma, and C. A. Grimes, "Synthesis of ordered arrays of discrete, partially crystalline titania nanotubes by Ti anodization using diethylene glycol electrolytes," *Journal of Materials Chemistry*, vol. 18, no. 28, pp. 3332–3336, 2008.

[32] S. Yoriya, M. Paulose, O. K. Varghese, G. K. Mor, and C. A. Grimes, "Fabrication of vertically oriented TiO_2 nanotube arrays using dimethyl sulfoxide electrolytes," *Journal of Physical Chemistry C*, vol. 111, no. 37, pp. 13770–13776, 2007.

[33] K. Shankar, G. K. Mor, A. Fitzgerald, and C. A. Grimes, "Cation effect on the electrochemical formation of very high aspect ratio TiO_2 nanotube arrays in formamide-water mixtures," *Journal of Physical Chemistry C*, vol. 111, no. 1, pp. 21–26, 2007.

[34] K. Shankar, G. K. Mor, H. E. Prakasam et al., "Highly-ordered TiO_2 nanotube arrays up to 220 μm in length: use in water photoelectrolysis and dye-sensitized solar cells," *Nanotechnology*, vol. 18, no. 6, Article ID 065707, 2007.

[35] O. K. Varghese, M. Paulose, and C. A. Grimes, "Long vertically aligned titania nanotubes on transparent conducting oxide for highly efficient solar cells," *Nature Nanotechnology*, vol. 4, no. 9, pp. 592–597, 2009.

[36] O. K. Varghese, D. Gong, M. Paulose, C. A. Grimes, and E. C. Dickey, "Crystallization and high-temperature structural stability of titanium oxide nanotube arrays," *Journal of Materials Research*, vol. 18, no. 1, pp. 156–165, 2003.

[37] C. A. Grimes and G. K. Mor, *TiO_2 Nanotube Arrays Synthesis, Properties, and Applications*, Springer, Berlin, Germany, 2009.

[38] G. K. Mor, K. Shankar, M. Paulose, O. K. Varghese, and C. A. Grimes, "High efficiency double heterojunction polymer photovoltaic cells using highly ordered TiO_2 nanotube arrays," *Applied Physics Letters*, vol. 91, no. 15, Article ID 152111, 2007.

[39] S. Günes, H. Neugebauer, and N. S. Sariciftci, "Conjugated polymer-based organic solar cells," *Chemical Reviews*, vol. 107, no. 4, pp. 1324–1338, 2007.

[40] S. A. Jenekhe and X. L. Chen, "Self-assembled aggregates of rod-coil block copolymers and their solubilization and encapsulation of Fullerenes," *Science*, vol. 279, no. 5358, pp. 1903–1907, 1998.

[41] G. Hadziioannou and F. von Hutten, *Semiconducting Polymers*, Wiley-VCH, Weinheim, Germany, 2000.

[42] N. S. Sariciftci and S. S. Sun, *Organic Photovoltaics*, Taylor & Francis, London, UK, 2005.

[43] A. Tracz, J. K. Jeszka, M. D. Watson, W. Pisula, K. Müllen, and T. Pakula, "Uniaxial alignment of the columnar superstructure of a hexa (alkyl) hexa-peri-hexabenzocoronene on untreated glass by simple solution processing," *Journal of the American Chemical Society*, vol. 125, no. 7, pp. 1682–1683, 2003.

[44] K. M. Coakley and M. D. McGehee, "Photovoltaic cells made from conjugated polymers infiltrated into mesoporous titania," *Applied Physics Letters*, vol. 83, no. 16, pp. 3380–3382, 2003.

[45] K. Shankar, G. K. Mor, M. Paulose, O. K. Varghese, and C. A. Grimes, "Effect of device geometry on the performance of TiO_2 nanotube array-organic semiconductor double heterojunction solar cells," *Journal of Non-Crystalline Solids*, vol. 354, no. 19–25, pp. 2767–2771, 2008.

[46] K. Shankar, G. K. Mor, H. E. Prakasam, O. K. Varghese, and C. A. Grimes, "Self-assembled hybrid polymer-TiO_2 nanotube array heterojunction solar cells," *Langmuir*, vol. 23, no. 24, pp. 12445–12449, 2007.

[47] D. C. Olson, J. Piris, R. T. Collins, S. E. Shaheen, and D. S. Ginley, "Hybrid photovoltaic devices of polymer and ZnO nanofiber composites," *Thin Solid Films*, vol. 496, no. 1, pp. 26–29, 2006.

[48] J. Y. Kim, S. H. Kim, H. H. Lee et al., "New architecture for high-efficiency polymer photovoltaic cells using solution-based titanium oxide as an optical spacer," *Advanced Materials*, vol. 18, no. 5, pp. 572–576, 2006.

[49] J. Peet, J. Y. Kim, N. E. Coates et al., "Efficiency enhancement in low-bandgap polymer solar cells by processing with alkane dithiols," *Nature Materials*, vol. 6, no. 7, pp. 497–500, 2007.

[50] K. M. Coakley, Y. Liu, M. D. McGehee, K. L. Frindell, and G. D. Stucky, "Infiltrating semiconducting polymers into self-assembled mesoporous titania films for photovoltaic applications," *Advanced Functional Materials*, vol. 13, no. 4, pp. 301–306, 2003.

[51] S. Kim, G. K. Mor, M. Paulose, O. K. Varghese, K. Shankar, and C. A. Grimes, "Broad spectrum light harvesting in TiO_2 nanotube array hemicyanine dye P3HT hybrid solid-state solar cells," *IEEE Journal on Selected Topics in Quantum Electronics*, vol. 16, no. 6, pp. 1573–1580, 2010.

[52] K. M. Coakley and M. D. McGehee, "Conjugated polymer photovoltaic cells," *Chemistry of Materials*, vol. 16, no. 23, pp. 4533–4542, 2004.

[53] F. Nuesch, J. E. Moser, V. Shklover, and M. Gratzel, "Merocyanine aggregation in mesoporous networks," *Journal of the American Chemical Society*, vol. 118, no. 23, pp. 5420–5431, 1996.

[54] G. K. Mor, O. K. Varghese, M. Paulose, K. Shankar, and C. A. Grimes, "A review on highly ordered, vertically oriented TiO_2 nanotube arrays: fabrication, material properties, and solar energy applications," *Solar Energy Materials and Solar Cells*, vol. 90, no. 14, pp. 2011–2075, 2006.

[55] K. M. Coakley, B. S. Srinivasan, J. M. Ziebarth, C. Goh, Y. Liu, and M. D. McGehee, "Enhanced hole mobility in regioregular polythiophene infiltrated in straight nanopores," *Advanced Functional Materials*, vol. 15, no. 12, pp. 1927–1932, 2005.

[56] T. A. Chen, X. Wu, and R. D. Rieke, "Regiocontrolled synthesis of poly(3-alkylthiophenes) mediated by Rieke zinc: their characterization and solid-state properties," *Journal of the American Chemical Society*, vol. 117, no. 1, pp. 233–244, 1995.

[57] W. Ma, C. Yang, X. Gong, K. Lee, and A. J. Heeger, "Thermally stable, efficient polymer solar cells with nanoscale control of the interpenetrating network morphology," *Advanced Functional Materials*, vol. 15, no. 10, pp. 1617–1622, 2005.

[58] T. Förster, "10th Spiers Memorial Lecture. Transfer mechanisms of electronic excitation," *Discussions of the Faraday Society*, vol. 27, pp. 7–17, 1959.

[59] Y. Liu, M. A. Summers, C. Edder, J. M. J. Fréchet, and M. D. McGehee, "Using resonance energy transfer to improve exciton harvesting in organic-inorganic hybrid photovoltaic cells," *Advanced Materials*, vol. 17, no. 24, pp. 2960–2964, 2005.

[60] C. X. Sheng, M. Tong, S. Singh, and Z. V. Vardeny, "Experimental determination of the charge/neutral branching ratio η in the photoexcitation of π -conjugated polymers by broadband ultrafast spectroscopy," *Physical Review B*, vol. 75, no. 8, Article ID 085206, 2007.

[61] S. R. Scully and M. D. McGehee, "Effects of optical interference and energy transfer on exciton diffusion length measurements in organic semiconductors," *Journal of Applied Physics*, vol. 100, no. 3, Article ID 034907, 2006.

[62] S. R. Scully, P. B. Armstrong, C. Edder, J. M. J. Fréchet, and M. D. McGehee, "Long-range resonant energy transfer for enhanced exciton harvesting for organic solar cells," *Advanced Materials*, vol. 19, no. 19, pp. 2961–2966, 2007.

[63] S. A. Haque, Y. Tachibana, R. L. Willis et al., "Parameters influencing charge recombination kinetics in dye-sensitized nanocrystalline titanium dioxide films," *Journal of Physical Chemistry B*, vol. 104, no. 3, pp. 538–547, 2000.

[64] R. Zhu, C. Y. Jiang, B. Liu, and S. Ramakrishna, "Highly efficient nanoporous TiO_2-polythiophene hybrid solar cells based on interfacial modification using a metal-free organic dye," *Advanced Materials*, vol. 21, no. 9, pp. 994–1000, 2009.

[65] C. Goh, S. R. Scully, and M. D. McGehee, "Effects of molecular interface modification in hybrid organic-inorganic photovoltaic cells," *Journal of Applied Physics*, vol. 101, no. 11, Article ID 114503, 2007.

[66] P. Liska, K. R. Thampi, M. Grätzel et al., "Nanocrystalline dye-sensitized solar cell/copper indium gallium selenide thin-film tandem showing greater than 15% conversion efficiency," *Applied Physics Letters*, vol. 88, no. 20, Article ID 203103, 2006.

[67] G. Yu, J. Gao, J. C. Hummelen, F. Wudl, and A. J. Heeger, "Polymer photovoltaic cells: enhanced efficiencies via a network of internal donor-acceptor heterojunctions," *Science*, vol. 270, no. 5243, pp. 1789–1791, 1995.

[68] Y. X. Liu, M. A. Summers, S. R. Scully, and M. D. McGehee, "Resonance energy transfer from organic chromophores to fullerene molecules," *Journal of Applied Physics*, vol. 99, no. 9, Article ID 093521, 2006.

[69] S. Lu and A. Madhukar, "Nonradiative resonant excitation transfer from nanocrystal quantum dots to adjacent quantum channels," *Nano Letters*, vol. 7, no. 11, pp. 3443–3451, 2007.

[70] J. Van de Lagemaat, K. D. Benkstein, and A. J. Frank, "Relation between particle coordination number and porosity in nanoparticle films: implications to dye-sensitized solar cells," *Journal of Physical Chemistry B*, vol. 105, no. 50, pp. 12433–12436, 2001.

[71] J. H. Yum, P. Walter, S. Huber et al., "Efficient far red sensitization of nanocrystalline TiO_2 films by an unsymmetrical squaraine dye," *Journal of the American Chemical Society*, vol. 129, no. 34, pp. 10320–10321, 2007.

[72] G. K. Mor, O. K. Varghese, M. Paulose, and C. A. Grimes, "Transparent highly ordered TiO2 nanotube arrays via anodization of titanium thin films," *Advanced Functional Materials*, vol. 15, no. 8, pp. 1291–1296, 2005.

[73] K. Shankar, J. Bandara, M. Paulose et al., "Highly efficient solar cells using TiO_2 nanotube arrays sensitized with a donor-antenna dye," *Nano Letters*, vol. 8, no. 6, pp. 1654–1659, 2008.

[74] U. Bach, D. Lupo, P. Comte et al., "Solid-state dye-sensitized mesoporous TiO_2 solar cells with high photon-to-electron conversion efficiencies," *Nature*, vol. 395, no. 6702, pp. 583–585, 1998.

[75] A. Inoue, T. Hosokawa, M. Haishi, and N. Ohtani, "4-(dicyanomethylene)-2-methyl-6-(p-dimethylaminostyryl)-4H-pyran (DCM)-doping density dependence of luminescence spectra and white emission in polymer light-emitting diodes," *Physica Status Solidi (C)*, vol. 6, no. 1, pp. 334–337, 2009.

[76] H. J. Snaith, A. Petrozza, S. Ito, H. Miura, and M. Graätzel, "Charge generation and photovoltaic operation of solid-state dye-sensitized solar cells incorporating a high extinction coefficient indolene-based sensitizer," *Advanced Functional Materials*, vol. 19, no. 11, pp. 1810–1818, 2009.

[77] H. J. Snaith, R. Humphry-Baker, P. Chen, I. Cesar, S. M. Zakeeruddin, and M. Grätzel, "Charge collection

and pore filling in solid-state dye-sensitized solar cells," *Nanotechnology*, vol. 19, no. 42, Article ID 424003, 2008.

[78] H. J. Snaith, A. J. Moule, C. Klein, K. Meerholz, R. H. Friend, and M. Grätzel, "Efficiency enhancements in solid-state hybrid solar cells via reduced charge recombination and increased light capture," *Nano Letters*, vol. 7, no. 11, pp. 3372–3376, 2007.

[79] W. M. Campbell, K. W. Jolley, P. Wagner et al., "Highly efficient porphyrin sensitizers for dye-sensitized solar cells," *Journal of Physical Chemistry C*, vol. 111, no. 32, pp. 11760–11762, 2007.

[80] D. M. Huang, H. J. Snaith, M. Grätzel, K. Meerholz, and A. J. MouÍ, "Optical description of solid-state dye-sensitized solar cells. II. Device optical modeling with implications for improving efficiency," *Journal of Applied Physics*, vol. 106, no. 7, Article ID 073112, 2009.

[81] R. H. Lohwasser, J. Bandara, and M. Thelakkat, "Tailor-made synthesis of poly(3-hexylthiophene) with carboxylic end groups and its application as a polymer sensitizer in solid-state dye-sensitized solar cells," *Journal of Materials Chemistry*, vol. 19, no. 24, pp. 4126–4130, 2009.

[82] H. Lee, H. C. Leventis, S. J. Moon et al., "PbS and CdS quantum dot-sensitized solid-state solar cells: "Old concepts, new results"," *Advanced Functional Materials*, vol. 19, no. 17, pp. 2735–2742, 2009.

[83] I. K. Ding, N. Tétreault, J. Brillet et al., "Pore-filling of spiro-OMeTAD in solid-state dye sensitized solar cells: quantification, mechanism, and consequences for device performance," *Advanced Functional Materials*, vol. 19, no. 15, pp. 2431–2436, 2009.

[84] D. Kuang, P. Walter, F. Nüesch et al., "Co-sensitization of organic dyes for efficient ionic liquid electrolyte-based dye-sensitized solar cells," *Langmuir*, vol. 23, no. 22, pp. 10906–10909, 2007.

[85] J. H. Yum, S. R. Jang, P. Walter et al., "Efficient co-sensitization of nanocrystalline TiO_2 films by organic sensitizers," *Chemical Communications*, no. 44, pp. 4680–4682, 2007.

[86] A. Burke, L. Schmidt-Mende, S. Ito, and M. Grätzel, "A novel blue dye for near-IR 'dye-sensitised' solar cell applications," *Chemical Communications*, no. 3, pp. 234–236, 2007.

[87] C. Siegers, U. Würfel, M. Zistler et al., "Overcoming kinetic limitations of electron injection in the dye solar cell via coadsorption and FRET," *ChemPhysChem*, vol. 9, no. 5, pp. 793–798, 2008.

[88] S. Honda, T. Nogami, H. Ohkita, H. Benten, and S. Ito, "Improvement of the light-harvesting efficiency in polymer/fullerene bulk heterojunction solar cells by interfacial dye modification," *ACS Applied Materials & Interfaces*, vol. 1, pp. 804–810, 2009.

[89] D. Poplavskyy and J. Nelson, "Nondispersive hole transport in amorphous films of methoxy-spirofluorene-arylamine organic compound," *Journal of Applied Physics*, vol. 93, no. 1, pp. 341–346, 2003.

[90] J. García-Cañadas, F. Fabregat-Santiago, H. J. Bolink, E. Palomares, G. Garcia-Belmonte, and J. Bisquert, "Determination of electron and hole energy levels in mesoporous nanocrystalline TiO_2 solid-state dye solar cell," *Synthetic Metals*, vol. 156, no. 14-15, pp. 944–948, 2006.

[91] U. B. Cappel, E. A. Gibson, A. Hagfeldt, and G. Boschloo, "Dye regeneration by Spiro-MeOTAD in solid state dye-sensitized solar cells studied by photoinduced absorption spectroscopy and spectroelectrochemistry," *Journal of Physical Chemistry C*, vol. 113, no. 15, pp. 6275–6281, 2009.

[92] J. Bourson and B. Valeur, "Ion-responsive fluorescent compounds. 2. Cation-steered intramolecular charge transfer in a crowned merocyanine," *Journal of Physical Chemistry*, vol. 93, no. 9, pp. 3871–3876, 1989.

[93] H. J. Snaith and L. Schmidt-Mende, "Advances in liquid-electrolyte and solid-state dye-sensitized solar cells," *Advanced Materials*, vol. 19, no. 20, pp. 3187–3200, 2007.

[94] T. Park, S. A. Haque, R. J. Potter, A. B. Holmes, and J. R. Durrant, "A supramolecular approach to lithium ion solvation at nanostructured dye sensitised inorganic/organic heterojunctions," *Chemical Communications*, vol. 9, no. 23, pp. 2878–2879, 2003.

[95] C. S. Karthikeyan and M. Thelakkat, "Key aspects of individual layers in solid-state dye-sensitized solar cells and novel concepts to improve their performance," *Inorganica Chimica Acta*, vol. 361, no. 3, pp. 635–655, 2008.

[96] J. Krüger, R. Plass, L. Cevey, M. Piccirelli, M. Grätzel, and U. Bach, "High efficiency solid-state photovoltaic device due to inhibition of interface charge recombination," *Applied Physics Letters*, vol. 79, no. 13, pp. 2085–2087, 2001.

[97] H. J. Snaith and M. Grätzel, "Enhanced charge mobility in a molecular hole transporter via addition of redox inactive ionic dopant: Implication to dye-sensitized solar cells," *Applied Physics Letters*, vol. 89, no. 26, Article ID 262114, 2006.

[98] E. T. Hoke, B. E. Hardin, and M. D. McGehee, "Modeling the efficiency of Förster resonant energy transfer from energy relay dyes in dyesensitized solar cells," *Optics Express*, vol. 18, no. 4, pp. 3893–3904, 2010.

[99] M. Grätzel, "Conversion of sunlight to electric power by nanocrystalline dye-sensitized solar cells," *Journal of Photochemistry and Photobiology A*, vol. 164, no. 1–3, pp. 3–14, 2004.

[100] G. Rottenkolber, R. Meier, O. Schafer, S. Wachter, K. Dullenkopf, and S. Wittig, *Laser Techniques for Fluid Dynamics*, R. J. Adrian, D. F. G. Durao, F. Durst, M. V. Heitor, M. Maeda and J. H. Whitelaw, Eds, Springer, Berlin, Germany, 2002.

[101] J. R. Lakowicz, *Principles of Fluorescence Spectroscopy*, Springer, Berlin, Germany, 3rd edition, 2006.

[102] K. Shankar, J. Bandara, M. Paulose et al., "Highly efficient solar cells using TiO_2 nanotube arrays sensitized with a donor-antenna dye," *Nano Letters*, vol. 8, no. 6, pp. 1654–1659, 2008.

[103] H. Kuhn, "Classical aspects of energy transfer in molecular systems," *The Journal of Chemical Physics*, vol. 53, no. 1, pp. 101–108, 1970.

[104] B. Wenger, M. Grätzel, and J.-E. Moser, "Rationale for kinetic heterogeneity of ultrafast light-induced electron transfer from Ru(II) complex sensitizers to nanocrystalline TiO_2," *Journal of the American Chemical Society*, vol. 127, no. 35, pp. 12150–12151, 2005.

[105] M. Ikeda, N. Koide, L. Han, A. Sasahara, and H. Onishi, "Scanning tunneling microscopy study of black dye and deoxycholic acid adsorbed on a rutile $TiO_2(110)$," *Langmuir*, vol. 24, no. 15, pp. 8056–8060, 2008.

[106] D. A. Fernández, J. Awruch, and L. E. Dicelio, "Photophysical and aggregation studies of t-butyl-substituted Zn phthalocyanines," *Photochemistry and Photobiology*, vol. 63, no. 6, pp. 784–792, 1996.

[107] M. K. Nazeeruddin, F. De Angelis, S. Fantacci et al., "Combined experimental and DFT-TDDFT computational

study of photoelectrochemical cell ruthenium sensitizers," *Journal of the American Chemical Society*, vol. 127, no. 48, pp. 16835–16847, 2005.

[108] M. K. Nazeeruddin, A. Kay, I. Rodicio et al., "Conversion of light to electricity by cis-X_2bis(2,2'-bipyridyl-4,4'-dicarboxylate)ruthenium(II) charge-transfer sensitizers (X = Cl^-, Br^-, I^-, CN^-, and SCN^-) on nanocrystalline TiO_2 electrodes," *Journal of the American Chemical Society*, vol. 115, no. 14, pp. 6382–6390, 1993.

[109] A. C. Fisher, L. M. Peter, E. A. Ponomarev, A. B. Walker, and K. G. U. Wijayantha, "Intensity dependence of the back reaction and transport of electrons in dye-sensitized nanocrystalline TiO_2 Solar Cells," *Journal of Physical Chemistry B*, vol. 104, no. 5, pp. 949–958, 2000.

[110] M. Law, L. E. Greene, J. C. Johnson, R. Saykally, and P. Yang, "Nanowire dye-sensitized solar cells," *Nature Materials*, vol. 4, no. 6, pp. 455–459, 2005.

[111] M. Adachi, Y. Murata, I. Okada, and S. Yoshikawa, "Formation of titania nanotubes and applications for dye-sensitized solar cells," *Journal of the Electrochemical Society*, vol. 150, no. 8, pp. G488–G493, 2003.

[112] O. K. Varghese, M. Paulose, T. J. LaTempa, and C. A. Grimes, "High-rate solar photocatalytic conversion of CO_2 and water vapor to hydrocarbon fuels," *Nano Letters*, vol. 9, no. 2, pp. 731–737, 2009.

[113] C. S. Karthikeyan, H. Wietasch, and M. Thelakkat, "Highly efficient solid-state dye-sensitized TiO_2 solar cells using donor-antenna dyes capable of multistep charge-transfer cascades," *Advanced Materials*, vol. 19, no. 8, pp. 1091–1095, 2007.

[114] S. Handa, H. Wietasch, M. Thelakkat, J. R. Durrant, and S. A. Haque, "Reducing charge recombination losses in solid state dye sensitized solar cells: the use of donor-acceptor sensitizer dyes," *Chemical Communications*, no. 17, pp. 1725–1727, 2007.

[115] S. A. Haque, S. Handa, K. Peter, E. Palomares, M. Thelakkat, and J. R. Durrant, "Supermolecular control of charge transfer in dye-sensitized nanocrystalline TiO_2 films: towards a quantitative structure-function relationship," *Angewandte Chemie - International Edition*, vol. 44, no. 35, pp. 5740–5744, 2005.

[116] C. S. Karthikeyan, K. Peter, H. Wietasch, and M. Thelakkat, "Highly efficient solid-state dye-sensitized TiO_2 solar cells via control of retardation of recombination using novel donor-antenna dyes," *Solar Energy Materials and Solar Cells*, vol. 91, no. 5, pp. 432–439, 2007.

[117] A. Zaban, S. G. Chen, S. Chappel, and B. A. Gregg, "Bilayer nanoporous electrodes for dye sensitized solar cells," *Chemical Communications*, no. 22, pp. 2231–2232, 2000.

[118] S. G. Chen, S. Chappel, Y. Diamant, and A. Zaban, "Preparation of Nb2O5 coated TiO_2 nanoporous electrodes and their application in dye-sensitized solar cells," *Chemistry of Materials*, vol. 13, no. 12, pp. 4629–4634, 2001.

[119] U. Diebold, "The surface science of titanium dioxide," *Surface Science Reports*, vol. 48, no. 5–8, pp. 53–229, 2003.

[120] C. Bauer, G. Boschloo, E. Mukhtar, and A. Hagfeldt, "Electron injection and recombination in $Ru(dcbpy)_2(NCS)_2$ sensitized nanostructured Zno," *Journal of Physical Chemistry B*, vol. 105, no. 24, pp. 5585–5588, 2001.

[121] T. P. Chou, Q. Zhang, and G. Cao, "Effects of dye loading conditions on the energy conversion efficiency of ZnO and TiO_2 dye-sensitized solar cells," *Journal of Physical Chemistry C*, vol. 111, no. 50, pp. 18804–18811, 2007.

[122] N. G. Park, J. Van De Lagemaat, and A. J. Frank, "Comparison of dye-sensitized rutile- and anatase-based TiO_2 solar cells," *Journal of Physical Chemistry B*, vol. 104, no. 38, pp. 8989–8994, 2000.